



# The Observed Spatiotemporal Variability of Antarctic Winter Water

T. Spira<sup>1</sup> , S. Swart<sup>1,2</sup> , I. Giddy<sup>1</sup> , and M. du Plessis<sup>1</sup> 

<sup>1</sup>Department of Marine Sciences, University of Gothenburg, Gothenburg, Sweden, <sup>2</sup>Department of Oceanography, University of Cape Town, Rondebosch, South Africa

### Key Points:

- Seasonal climatologies of Antarctic Winter Water (WW) and its properties are mapped using 18 years of in situ observations
- Observations reveal the distinct seasonal and regional characteristics of WW and their potential link to processes such as sea ice formation
- Localized redistribution of WW properties equatorward is steered by large topographic features

### Supporting Information:

Supporting Information may be found in the online version of this article.

### Correspondence to:

T. Spira,  
[theo.spira@outlook.com](mailto:theo.spira@outlook.com)

### Citation:

Spira, T., Swart, S., Giddy, I., & du Plessis, M. (2024). The observed spatiotemporal variability of Antarctic Winter Water. *Journal of Geophysical Research: Oceans*, 129, e2024JC021017. <https://doi.org/10.1029/2024JC021017>

Received 7 FEB 2024  
Accepted 25 SEP 2024

### Author Contributions:

**Conceptualization:** T. Spira, S. Swart, M. du Plessis

**Data curation:** T. Spira

**Formal analysis:** T. Spira

**Funding acquisition:** S. Swart, M. du Plessis

**Investigation:** T. Spira, S. Swart, I. Giddy, M. du Plessis

**Methodology:** T. Spira, S. Swart, I. Giddy, M. du Plessis

**Project administration:** S. Swart, M. du Plessis

**Resources:** T. Spira, S. Swart, M. du Plessis

**Software:** T. Spira

**Supervision:** S. Swart, M. du Plessis

© 2024. The Author(s).

This is an open access article under the terms of the [Creative Commons Attribution License](https://creativecommons.org/licenses/by/4.0/), which permits use, distribution and reproduction in any medium, provided the original work is properly cited.

**Abstract** The Southern Ocean (SO) is central to the global overturning circulation. South of the Antarctic Polar Front, Antarctic Winter Water (WW) forms in the wintertime mixed layer (ML) and becomes a subsurface layer following summertime restratification of the ML, overlaying upwelled deep waters. Model simulations show that WW acts as a conduit to seasonally transform upwelled deep waters into intermediate waters. Yet, there remains little observational evidence of the distribution and seasonal characteristics of WW. Using 18 years of in situ observations, we show seasonal climatologies of WW thickness, depth, core temperature, and salinity, revealing a distinct regionality and seasonality of WW. The seasonal cycle of WW characteristics is tied to the annual sea ice evolution, whereas the spatial distribution is impacted by the main topographic features in the SO driving an equatorward flux of WW. Through the identification of these localized northward export regions of WW, this study provides further evidence suggesting an alternative view from the conventional “zonal mean” perspective of the overturning circulation. We show that specific overturning pathways connecting the subpolar ocean to the global ocean can be explained by ocean-topography interactions.

**Plain Language Summary** The Southern Ocean (SO) around Antarctica is central to the global ocean circulation system. The cold wintertime atmosphere drives ocean cooling and sea ice formation, which causes surface waters to become denser, mixing with deep waters that rise to the surface from the deep ocean. As the ocean surface layer warms in summer, there remains a cold layer below the surface known as Antarctic Winter Water (WW). This layer warms throughout the summer, thinning the WW layer. However, the properties of WW (temperature, salinity, thickness, and depth) vary in space and in erosion rate around the SO. By compiling 18 years of ocean observations, we investigate the physical dynamics that determine how WW changes in space and over the average annual cycle. We find that there are localized regions across the SO where WW properties are transported northward as part of the ocean circulation system, which typically aligns with large topographic features and acts to connect SO water masses to the global ocean.

## 1. Introduction

The Southern Ocean (SO) is characterized by the zonally unbounded energetic flow of the Antarctic Circumpolar Current (ACC), which consists of several jets that delineate hydrographic properties (Orsi et al., 1995). South of the Antarctic Polar Front (PF), salinity is the dominant property of density in the upper ocean due to a low thermal expansion coefficient (Roquet et al., 2022; Stewart & Haine, 2016). Consequently, this allows for the formation of a cold subsurface layer known as Antarctic Winter Water (WW) that resides below the summertime mixed layer (ML) (Toole, 1981).

WW lies above the salty and relatively warmer Circumpolar Deep Water (CDW), which has been upwelled along isopycnals from the low latitude deep ocean (Tamsitt et al., 2017). CDW gets transformed to become either dense bottom water, sinking back to the abyssal ocean (Ganachaud & Wunsch, 2000; Jacobs, 2004; van Sebille et al., 2013) or transformed to intermediate water north of the ACC (Munk, 1966; Whitworth et al., 1994). Using a general circulation model, Evans et al. (2018) showed that WW acts to diabatically transform CDW. In wintertime, CDW is freshened and cooled through entrainment into the WW surface layer. This WW-CDW mixture is subsequently warmed and freshened through summertime air-sea-ice buoyancy fluxes to contribute to the formation of Antarctic Intermediate Water, which, when subducted, forms the upper limb of the SO meridional overturning circulation (Marshall & Speer, 2012; Speer et al., 2000; Talley, 2013). Water mass transformation in the upper SO is associated with net freshening due to sea ice export and melt (Abernathey et al., 2016; Pellichero et al., 2018; Klocker et al., 2023), and Tamsitt et al. (2018) showed that upwelled CDW

**Visualization:** T. Spira, S. Swart, M. du Plessis  
**Writing – original draft:** T. Spira  
**Writing – review & editing:** T. Spira, S. Swart, I. Giddy, M. du Plessis

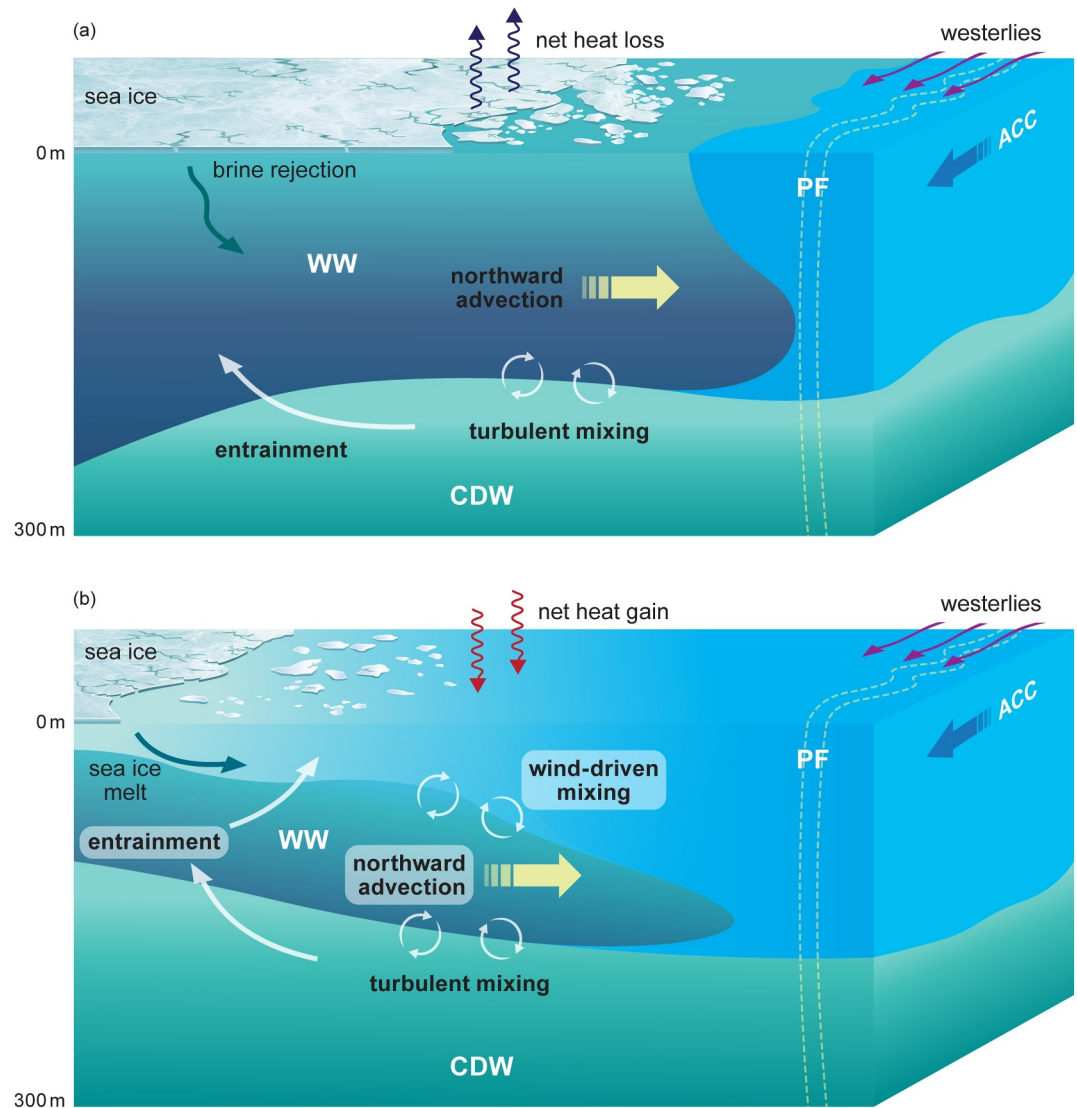


**Figure 1.** Conceptual view of Antarctic Winter Water (WW). (a) Mixed layer (ML) WW in wintertime and (b) Subsurface WW in summertime following summertime ML restratification. Shown are the various physical mechanisms that impact the formation, distribution, and erosion of WW. In panel (b), we highlight the terms that we investigate in the heat budget (Sections 2.3 and 3.1.4).

becomes fresher and colder before transforming into intermediate waters, further implying the seasonal role of WW in the overturning circulation. Drake et al. (2018) show through the investigation of Lagrangian pathways that CDW upwelling is not well represented via the time mean overturning framework, and thus a similar argument likely applies to the representation of WW in the same zonally integrated overturning framework. Given these findings, the evolution and characteristics of WW are important to the overall SO's role in the global overturning circulation.

WW forms in the wintertime mixed layer (ML; Figure 1a) (Hoppema et al., 1995; Mosby, 1934; Sharma & Mathew, 1985) with WW temperature set by intense wintertime air-sea heat loss. Subsequent brine rejection from sea ice formation deepens the under-ice ML, driving entrainment of the warm subsurface CDW and thus increases ML heat and salinity (Gordon & Huber, 1984; Martinson, 1990). In turn, this melts sea ice and freshens the ML to reduce its buoyancy; thus, through this feedback system, sea ice thickness is modulated (Shaw & Stanton, 2014) and the under-ice ML depth is confined to less than 200 m (Biddle & Swart, 2020; Wilson et al., 2019). Following a change in sign of the atmospheric heat flux, the summertime ML shoals becoming warm and fresh with a depth

of only tens of meters (Pellichero et al., 2017), leaving a residual subsurface cold wintertime ML below the summer-warmed surface layer (Figure 1b) and thus creating a warm-cold-warm layering of ML-WW-CDW (Park, Charriaud, & Fieux, 1998).

Eventually, WW erodes over the annual cycle or is re-entrained into the following winter ML. Giddy et al. (2023) found that WW erosion rates are primarily driven by entrainment of WW into the ML through mechanical mixing, with further warming due to double diffusive convection from below. However, these findings are specific to the Weddell Sea where there is typically a sharp thermocline yet a weak pycnocline (Wilson et al., 2019), which impacts the temperature gradient as well as the rate of mixing that takes place. Further, the variability of WW properties have been observed in regions up and downstream of large topographic features that interact with the ACC, enhancing the downstream mesoscale field, such as that found by Sabu et al. (2020). Lund et al. (2021) show similar spatial variability across the circumpolar SO via climatological WW temperatures. Sabu et al. (2020) also observe the WW layer responding to large-scale atmospheric variability, finding enhanced warming in years of positive Southern Annular Mode, likely due to elevated wind-driven mixing from stronger winds. The variability of WW observed is tied to various mechanisms that impact upper ocean structure, such as varying eddy kinetic energy (Dove et al., 2022; Nikurashin et al., 2013), differing wind stress fields (Abernathy et al., 2011; Lin et al., 2018), and CDW outcropping pathways (Narayanan et al., 2023; Tamsitt et al., 2021).

In this study, we provide revised criteria for defining the vertical distribution of WW. We apply this to 18 years of in situ observations over the SO to examine the spatiotemporal distribution of WW, its properties using seasonal climatologies, and the dynamics governing these distributions. A seasonally evolving heat budget for WW is estimated to shed light on the dominating processes, which impact the evolution and erosion of WW, and to better understand its connection to the surface layer of the ocean and meridional circulation. Finally, we reveal linkages between WW distribution and its properties to the underlying topography of the SO. WW seasonality and spatial distribution plays a key role in the upper limb of the overturning circulation system, so determining possible pathways of enhanced overturning is critically important in understanding our global climate and the redistribution of oceanic properties.

## 2. Data and Methods

### 2.1. Hydrographic Profiles

This study uses hydrographical profiles south of 40°S from the period 2004 to 2021 compiled using the Argo float data set (Wong et al., 2020), tagged marine seals data set (MEOP: Marine Mammals Exploring the Oceans Pole to Pole) (Treasure et al., 2017) as well as ship-based CTD casts and glider profiles (from WOD18: The World Ocean Database 2018) (Boyer et al., 2018). It is worthwhile noting that SO biogeochemical floats (SOCCOM: SO Carbon and Climate Observations and Modeling) (SOCCOM, 2019) are incorporated and are a main contributor to the SO Argo data set. Data are relatively well distributed across the SO due to sampling from the Argo and MEOP programs (Figures 2e–2h), which are extensive compared to limited historical CTD ship-based data collection (Brett et al., 2020). The Pacific sector is mainly sampled throughout the annual cycle via the Argo program, whereas MEOP data cover a great extent south of the PF, particularly in the Atlantic and Indian Ocean sectors as well as below sea ice and across the circumpolar continental shelf (Narayanan et al., 2023). MEOP seals are tagged in the summertime, so they provide least coverage in spring after CTD sensors have dropped off the seals from molting their winter fur, whereas their habitat location and foraging behavior largely dictate their spatial distribution (McMahon et al., 2019).

Additionally, the location of float sampling is initially spatially biased to deployment location due to ship-based deployments and subsequently follow quasi-Lagrangian trajectories. Therefore, float data are heterogeneously distributed in space and time (Figures 2a–2d) with different regions sampled in different time periods. There are fewer total profiles per month from 2020 and onward (Figure 2i) because of limited scientific cruises during the global pandemic (Boyer et al., 2023; Sarmiento et al., 2023). Consequently, there are limited MEOP data in 2020 and 2021, but the remaining operating floats continued to sample the SO.

In sea-ice-covered regions, ship-based measurements are geographically accurate as they contain GPS fixes; seal-based locations, however, are not geographically accurate when they are under sea ice or diving. Profiling floats use a temperature-based sea ice avoidance algorithm and similarly, they cannot transmit their location when under sea ice and only transmit their location once they surface either when sea ice retreats or when in ice-free ocean. In



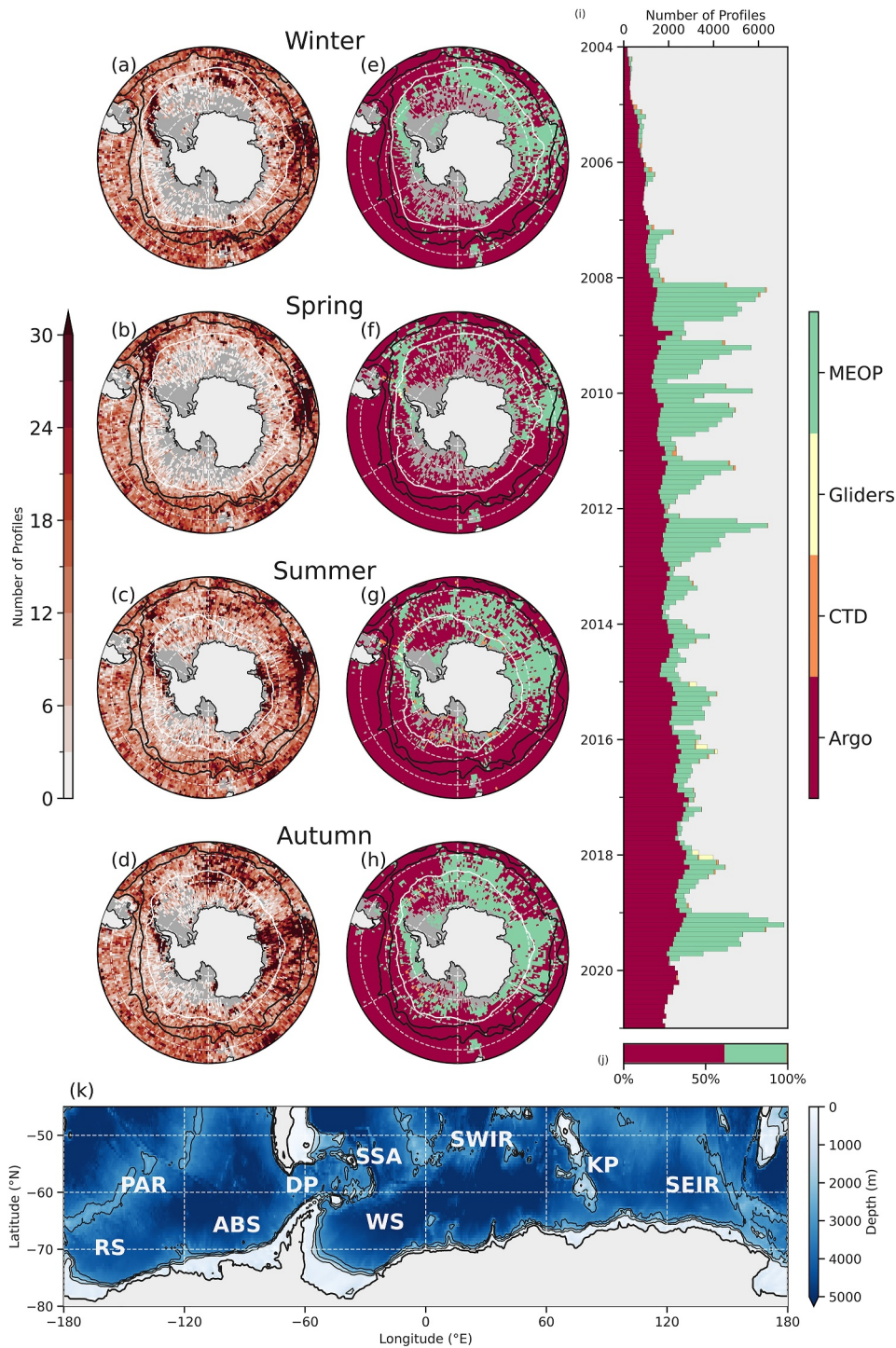


**Figure 2.** Hydrographic data distributions. (a–d) Spatial distribution of the total number of hydrographic profiles per austral season from winter to autumn, respectively. (e–h) Spatial distribution of the mode data source per grid cell. The black contours indicate the Polar Front and Subantarctic Front, and the white lines are the mean 15% sea ice concentration for the relevant season in panels (a–h). (i) Monthly time series of data sources (stacked) across the Southern Ocean (SO). (j) Total proportion of data per data source as a percentage. (k) SO bathymetry map with bathymetric features and seas. Thin black lines denote 1, 2, and 3 km bathymetric contours. Abbreviations are as follows: RS, Ross Sea; PAR, Pacific-Antarctic Ridge; ABS, Amundsen and Bellingshausen Seas; DP, Drake Passage; SSA, South Sandwich Arch; WS, Weddell Sea; SWIR, Southwest Indian Ridge; KP, Kerguelen Plateau; SEIR, Southeast Indian Ridge. White dashed lines in panels (a–h) and (k) represent latitudes of 80, 70, 60, 50°S and longitudes of –180, –120, –60, 0, 60, 120, 180°E.



these regions, float locations are linearly interpolated. For this study, we use this data but are cognizant that the climatologies may contain systematic errors, such as regional biases and inaccuracies in computed variables (Oke et al., 2022; Reeve et al., 2015; Zilberman et al., 2017).

Float-based measurements of temperature and salinity have been corrected for any sensor biases in real time and undergo delayed mode quality control testing (Wong et al., 2020). We only use data flagged as “good” or “under sea-ice” for all data sources. Following Wilson et al. (2019), we further quality control the data such that each profile contains at least five measurements in the top 300 dbar with at least one data point in the top 25 dbar to ensure representation of the upper ocean processes of interest, ensuring both the ML and majority of WW properties are captured. Profiles containing unrealistic values of potential temperature and practical salinity are removed such that  $-2.5^{\circ}\text{C} < T < 16^{\circ}\text{C}$  and  $30 < S < 36$ . These thresholds are obtained from the observed range of properties south of the Subantarctic Front. Consequently, in this study, we analyze 620,293 quality-controlled CTD profiles.

The profiles are linearly interpolated to a standard two dbar vertical grid followed by a one-dimensional Gaussian filter with a standard deviation of four to smooth the data but retain key features. Absolute Salinity and Conservative Temperature  $\theta$  are derived from these gridded, quality controlled and smoothed profiles. The WW detection algorithm (Section 2.2) is applied to each profile, with all depth-related variables converted to meters, before gridding the data onto a median  $1^{\circ} \times 1^{\circ}$  latitude-longitude seasonal climatology. Since the formation and annual cycle of the ML and, therefore, WW is influenced by sea ice evolution (Gordon & Huber, 1990; Pellichero et al., 2017), we define the climatological seasons based on the annual cycle of sea ice formation and melt such that January, February, and March represent austral summer and so on (Goosse et al., 2023; Holland, 2014).

## 2.2. Antarctic Winter Water Algorithm

WW definitions vary in present literature. Park, Charriaud, Pino, and Jeandel (1998) define WW as a relatively homogeneous subsurface layer south of the PF with a subsurface temperature minimum, defining the upper boundary with a strong hydrographic gradient (thermo-, halo-, pycnocline) and the lower boundary as strong temperature and salinity gradients. Evans et al. (2018) define WW via a temperature threshold such that  $\Theta < 0.5^{\circ}\text{C}$ . Sabu et al. (2020) define WW as the depth of the coldest temperature inversion observed below the ML. Giddy et al. (2023) use a definition that bounds the WW: the upper boundary as the ML depth (MLD), core depth as the temperature minimum below the MLD, and lower boundary as the max temperature gradient below the WW core, marking the transition from WW to CDW.

We characterize WW into two classifications: ML WW ( $\text{WW}_{\text{ML}}$ , Figures 1a and 4e) and subsurface WW ( $\text{WW}_{\text{SS}}$ , Figures 1b and 4f–4h).  $\text{WW}_{\text{ML}}$  is defined as constrained to the ML: we take the upper boundary as the ocean surface (0 m) and the ML depth (MLD) as the lower boundary. We assume the ML is well-mixed and therefore take the mid-depth of MLD as the WW core depth, whereas the core properties are defined as the mean properties across the ML.  $\text{WW}_{\text{SS}}$  only exists if there is a temperature inversion below the ML. Further,  $\text{WW}_{\text{SS}}$  only exists if there are at least 10 temperature inversions, equivalent to 20 m, below the ML. We found that this threshold suitably removes noisy profiles and keeps the majority of real WW profiles (see Figure S1 in Supporting Information S1 for further details). The  $\text{WW}_{\text{SS}}$  upper boundary is defined as the maximum temperature gradient below the ML and above the  $\text{WW}_{\text{SS}}$  core whereas the lower boundary is defined as the maximum temperature gradient below the  $\text{WW}_{\text{SS}}$  core. Using the maximum temperature gradient, similar to the maximum stratification, denotes the transition layer where active mixing takes place (Dohan & Davis, 2011). We describe  $\text{WW}_{\text{SS}}$  through its core properties (the temperature minimum, the depth at which the temperature minimum occurs as well as the salinity and density at that depth) and thickness (difference in depth between upper and lower boundary). We summarize the property definitions of the WW classifications in Figure 3. Note that we define the MLD following the density difference criterion of  $0.03\text{ kg m}^{-3}$  from a reference density taken from the surface at 10 dbar, as per de Boyer Montégut (2004).

WW only exists if the core temperature is below  $2^{\circ}\text{C}$  since this temperature denotes the boundary for the PF at 200 m depth (Belkin & Gordon, 1996; Morrow et al., 2008; Pollard et al., 2002). The PF is a baroclinic barrier to WW, marking the transition from subpolar ocean where salinity dominates the density signal (beta ocean) to the equatorward ocean where temperature dominates the density signal (alpha ocean), which determines the existence of temperature inversions (Caneill et al., 2024; Orsi et al., 1995; Stewart & Haine, 2016). If the temperature at the lower bound is warmer than  $2^{\circ}\text{C}$ , the  $2^{\circ}\text{C}$  isotherm depth is used as the WW lower boundary instead. Further, if

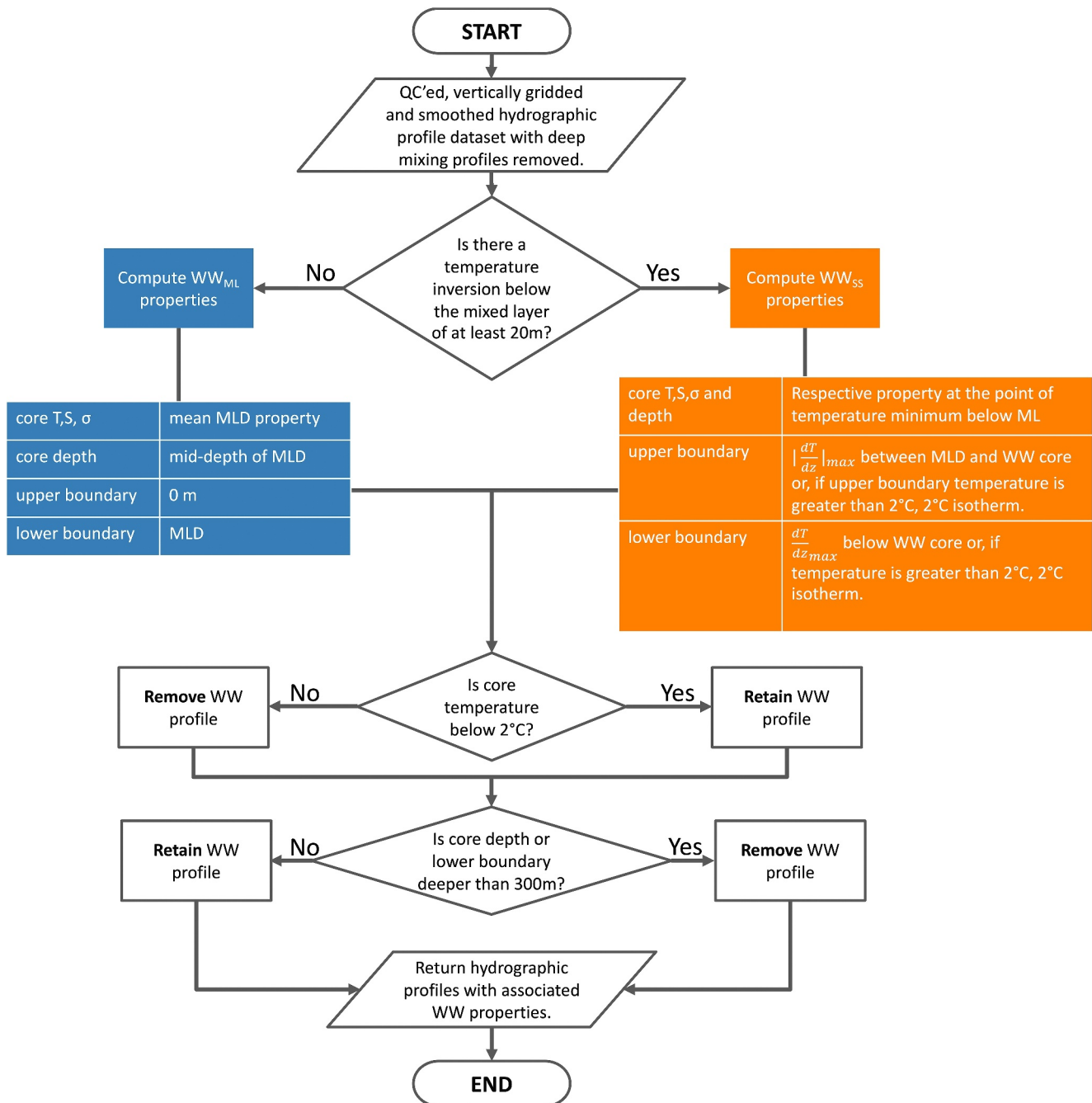


**Figure 3.** Antarctic Winter Water (WW) algorithm flowchart. A flowchart summarizing the algorithm used for Antarctic WW detection, where blue elements correspond with Mixed Layer WW and orange elements correspond with Subsurface WW.

the core depth is deeper than the lower bound depth, we conclude no WW exists in that profile. Similarly, if the core temperature is warmer than 2°C then we conclude no WW exists in that profile. The lower boundary or core depth of WW can feasibly reach depths below 300 m, for example, via deep convection cells as a result of polynya driven processes, which are typically found close to the Antarctic continent (Mohrmann et al., 2021; Morales Maqueda et al., 2004; Tamura et al., 2008; Whitworth et al., 1994). However, these processes are associated with deep water formation (Jacobs, 2004; Johnson, 2008; Kusahara et al., 2017; Meredith, 2013) and therefore associated with dynamics outside the scope of this study. Thus, we remove vertical profiles that are associated with deep mixing before WW computation, which are largely identified in the Mode Water deep mixing bands

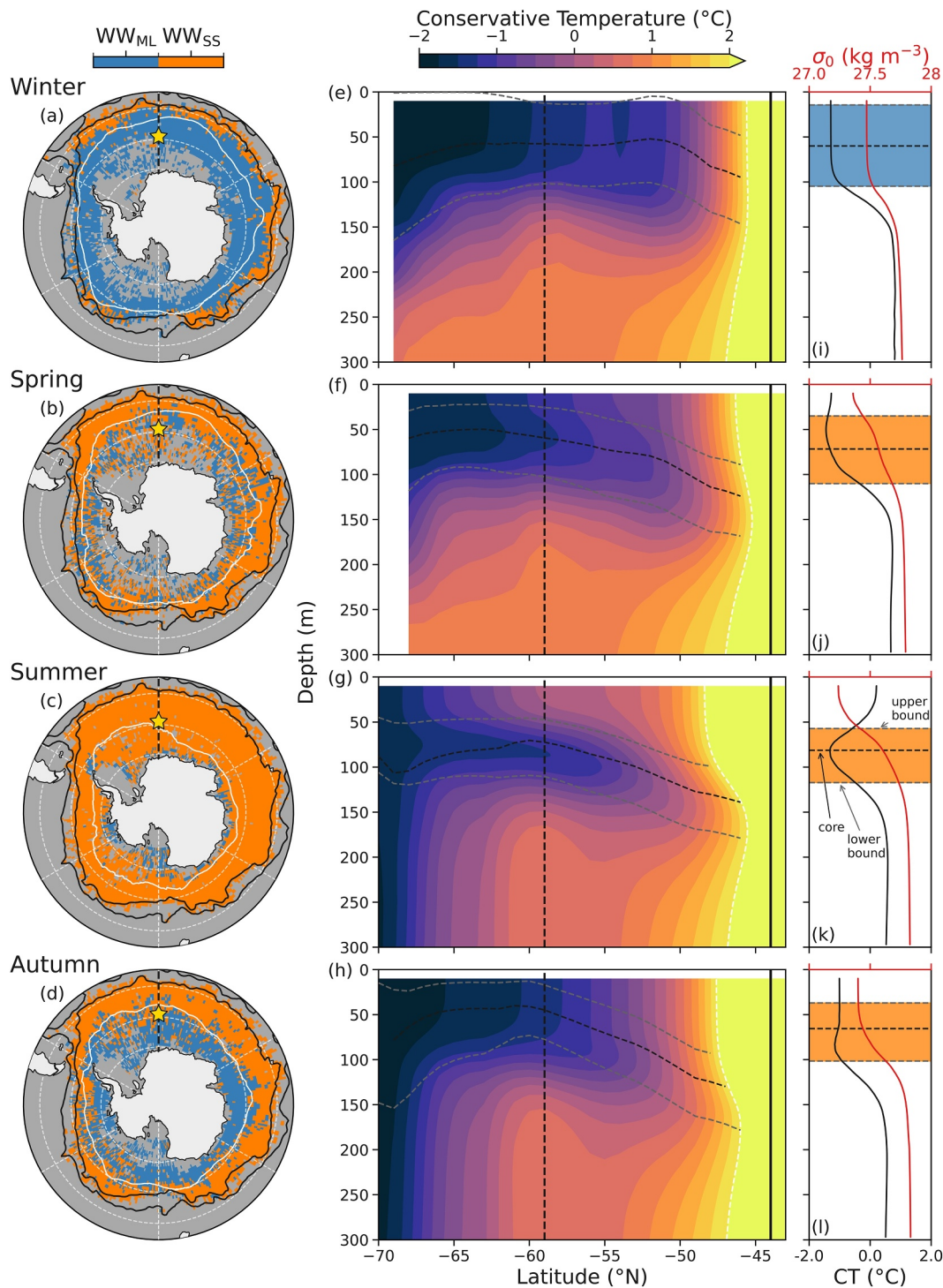


**Figure 4.** Antarctic Winter Water (WW) classification. (a–d) Spatial distribution of the mode classification of WW for each grid cell from winter through to autumn, respectively, where blue (orange) represents WW<sub>ML</sub> (WW<sub>SS</sub>) profiles. The black lines denote the PF and SAF of the Antarctic Circumpolar Current, the white lines show the seasonal mean 15% sea ice concentration, and dashed white lines represent latitudes of 80, 70, 60, 50°S and longitudes of –180, –120, –60, 0, 60, 120, 180°E; the dotted black line shows the cross-section location in panels (e–h) and the star denotes the profiles in panels (i–l). (e–h) Smoothed meridional cross-section along 0°E for each season. The solid black vertical lines denote the PF; the light gray dashed lines denote the upper and lower bounds of WW, the black dashed line denotes the WW core, and the white dashed line denotes the 2°C isotherm. The dotted black lines show the location of the star in panels (a–d) and are the profiles shown in panels (i–l). (i–l) Show profiles of conservative temperature (black) and potential density (red) from the location 59°S, 0°E throughout the seasonal cycle. The light gray dashed lines denote the upper and lower bounds of WW, and the black dashed line denotes the WW core as in panels (e–h). The classification is shown by shading: blue (orange) shading represents WW<sub>ML</sub> (WW<sub>SS</sub>) profiles, as in panels (a–d).



(which are usually located north of the PF) and close to the Antarctic continent. WW is otherwise typically found in the bounds of 50–200 m (Lund et al., 2021; Sabu et al., 2020), so WW profiles with a lower boundary or core depth deeper than 300 m are removed.

In total, 39% of the 620,293 profiles poleward of 40°S contains WW, equating to 241,115 WW profiles detected and consisting of 107,986 WW<sub>ML</sub> profiles and 133,129 WW<sub>SS</sub> profiles (Figures 4a–4d). We then compute the climatologies, which are smoothed using a 3° × 3° latitude-longitude rolling mean and interpolated across a maximum gap of three missing grid cells to the maximum WW extent.

### 2.3. Temperature Tendency

Adapting the temperature tendency equation of Giddy et al. (2023) to Equation 1, we compute a temperature tendency of WW<sub>SS</sub> to investigate the dynamics that impact how WW evolves and erodes over the annual cycle. We focus on the temperature evolution since that is the defining criterion determining the existence of WW<sub>SS</sub>; this allows us to better understand the physical mechanisms impacting the seasonal evolution of WW<sub>SS</sub>. Further, we focus on WW<sub>SS</sub> since it is this part of the seasonal cycle that potentially connects CDW to intermediate waters in the upper limb of the meridional overturning circulation system, as described by Evans et al. (2018). Since this budget investigates only WW<sub>SS</sub> and does not include the formation period of WW in the ML (WW<sub>ML</sub>), we neglect air-sea heat fluxes in the budget computation since the water mass does not directly interact with the atmosphere. Similarly, Ekman fluxes are not considered (including Ekman pumping) since they play a larger role in the layer above WW<sub>SS</sub>; Giddy et al. (2023) showed that vertical Ekman velocities are two orders of magnitude lower than entrainment velocities.

$$\underbrace{\frac{\delta}{\delta t}(T_{SS})}_{(I)} = \frac{1}{\rho_0 C_p h_{SS}} \left( \underbrace{\Delta Q_{SW}}_{(II)} + \underbrace{Q_{\text{mixing}}}_{(III)} + \underbrace{Q_{\text{entrainment}}}_{(IV)} + \underbrace{Q_{\text{subduction/obduction}}}_{(V)} + \underbrace{Q_{\text{residual}}}_{(VI)} \right) \quad (1)$$

Each term is normalized by WW thickness ( $h_{SS}$ ), so that Equation 1 represents a change in mean temperature across the WW<sub>SS</sub> water column.

Term (I) is the temperature tendency of the WW<sub>SS</sub> system, which can be calculated by taking the time derivative from season to season of the integrated heat content (Huguenin et al., 2022) over the WW<sub>SS</sub> layer. The integrated heat content is computed such that

$$T_{SS} = \frac{1}{h_{SS}} \int^{\text{thickness}} \Theta^* \delta z$$

where  $h_{SS}$  is the WW<sub>SS</sub> layer thickness and  $\Theta^*$  is the Conservative Temperature,  $\Theta$ , adjusted by the freezing point of seawater to negate sign errors. The time step,  $\frac{\delta}{\delta t}$ , represents the difference from one season to the next with a unit of seconds, which is computed as the mean number of seconds per season across the 2004–2021 period.

Term (II) represents the penetrative shortwave radiation (see Section 2.4 for details on the shortwave radiation data) absorbed by the WW layer, which is the difference in shortwave entering at the upper boundary and leaving at the lower boundary. This term is approximated via exponential decay of shortwave solar radiation from the surface using Jerlov water type II as per Paulson and Simpson (1977):

$$R_s(z) = R_s(0) \left[ 0.77 \exp\left(\frac{-|z|}{1.4}\right) + 0.23 \exp\left(\frac{-|z|}{14}\right) \right]$$

where  $R_s(z)$  is the net shortwave radiation at the depth  $z$  such that

$$Q_{SW} = R_s(z) - R_s(0).$$

Term (III) is the down-gradient turbulent heat flux term across the ML-WW interface due to wind-driven mechanical mixing. Nicholson et al. (2022) show a close correlation between theoretical and observed dissipation rates in SO boundary layer during summertime ( $r^2 = 0.75$ , see their Figure S5 in their Supporting Information S1). Hence, we calculate the diapycnal diffusivity,  $\kappa$ , such that

$$\kappa = \Gamma \frac{\varepsilon}{N^2}$$

where the mixing coefficient,  $\Gamma = 0.2$ , is a constant, which we take as the modified Osborn number for a transitional regime (Bouffard & Boegman, 2013; Gregg et al., 2018; Osborn, 1980). Assuming winds are the dominant driving factor, we approximate turbulence dissipation ( $\varepsilon$ ) at the base of the ML (i.e., the upper boundary of the WW) via law of the wall (von Kármán, 1931) such that  $\varepsilon = \frac{u_*^3}{kz}$ , using frictional velocity,  $u_* = \sqrt{\frac{\tau}{\rho_{sw}}}$ , where  $\tau$  is the climatological mean wind stress and  $\rho_{sw} = 1035 \text{ kg m}^{-3}$  is the reference density of seawater (Huguenin et al., 2022). Further, we use von Kármán's constant,  $k = 0.41$ , and  $z$  as the MLD.  $N^2$  is the stratification across the upper boundary of the WW<sub>SS</sub>. We use this to compute

$$Q_{\text{mixing}} = \frac{1}{h_{SS}} (\kappa \Delta T),$$

where  $\Delta T$  is the temperature difference between the ML and 20 m below the ML following ML entrainment methodology for computing temperature gradients - see further details on this methodology under Term (IV). See Section 2.4 for information on wind stress data.

Term (IV) measures the change in WW heat from entrainment and detrainment, which results in a flux of temperature at both the upper (ML-WW) and lower (WW-CDW) boundaries. Term (IV) is calculated using the general formula,  $Q_{\text{entrainment}} = \frac{H}{h} w_{eIF} \Delta T_{IF}$ , where  $H$  is the Heaviside function of vertical velocities such that

$$H(w_{eIF}) = \begin{cases} 0 & \text{if } w_{eIF} < 0, \\ 1 & \text{if } w_{eIF} > 0. \end{cases}$$

where  $w_{eIF} = \frac{dh}{dt}$  is the vertical velocity and  $IF$  is the interface between water masses. The temperature gradient,  $\Delta T$ , is taken across the ML-WW interface as the difference between the ML temperature and 15 m below the MLD (Pellichero et al., 2017; du Plessis et al., 2022). Across the WW-CDW layer, we use the average WW temperature minus the temperature 5 m below the WW, as per Giddy et al. (2023). Then, we compute the entrainment term using

$$Q_{\text{entrainment}} = \frac{H_{ub}}{h_{SS}} w_{e_{ub}} \Delta T_{ML-WW} + \frac{H_{lb}}{h_{SS}} w_{e_{lb}} \Delta T_{WW-CDW}.$$

Term (V) represents temperature change due to the subduction or obduction of WW<sub>SS</sub>. WW<sub>SS</sub> is subducted following the restratification of the wintertime ML, resulting in a warm and fresh summertime ML that caps a cold layer of remnant wintertime ML that we have defined as WW<sub>SS</sub>. WW<sub>SS</sub> is formed if there exists no WW<sub>SS</sub> in  $t_{i-1}$  and WW<sub>SS</sub> exists in  $t_i$  (where  $t$  is the season index), which results in an input of heat into the WW<sub>SS</sub> system. Conversely, we assume WW<sub>SS</sub> has been obducted if there is WW<sub>SS</sub> in  $t_{i-1}$  and no WW<sub>SS</sub> in  $t_i$ , which causes a cooling of WW<sub>SS</sub>. This physically represents the total WW<sub>SS</sub> erosion over the annual cycle or that WW<sub>ML</sub> formation obducts remaining WW<sub>SS</sub> by entraining into the wintertime ML. We introduce this term to parameterize the heat change associated with subduction and obduction of WW<sub>SS</sub> since the temporal resolution of the seasonal climatological data set in use does not allow for the direct observation of total erosion or re-entrainment of WW<sub>SS</sub>. We compute term (V) such that

$$Q_{\text{subduction/obduction}} = \frac{M}{h_{WW_i}} \frac{\delta}{\delta t} \left( \int^{\text{thickness}} \Theta^* \delta z \right)$$

where

$$M = \begin{cases} 1 & \text{if } |C(WW)_t - C(WW)_{t-1}| = 1 \\ 0 & \text{otherwise} \end{cases} \quad \text{and} \quad C(WW) = \begin{cases} 1 & \text{if } WW_{ML}, \\ 2 & \text{if } WW_{SS}. \end{cases}$$

Here,  $C(WW)$  determines the classification of WW ( $WW_{ML}$  or  $WW_{SS}$ ). Thus,  $M$  determines whether there has been a change in the WW classification.  $h_{WW_i}$  is the thickness of the WW based on classification (either  $WW_{ML}$  or  $WW_{SS}$ ). This term accounts for the one-dimensional vertical movement in time but does not account for any lateral movement that may result in a change in the WW classification.

Lastly, term (VI) is the residual and incorporates any processes not accounted for in the other terms, which includes (but is not limited to) mean shear, diffusive convection, small-scale processes, uncertainties in the calculated terms, vertical advection, and horizontal advection. Diffusive staircases perpetuate across large regions of the SO (van der Boog et al., 2021). While the resultant diffusive mixing is important for water mass transformation (Evans et al., 2018), the heat flux contribution remains small (Bebieva & Speer, 2019; Giddy et al., 2023; Wilson et al., 2019). Further, vertical processes, such as submesoscale motions, are not resolvable given the geostrophic scale of the gridded data set, meaning their attributed heat fluxes are not directly computable (Section 4.2) but are incorporated as part of the geostrophic mean field flux. Given the numerical findings of Morrison et al. (2016), who show a substantial northward heat flux by the mean flow, we assume that lateral advection dominates the residual term similar to Pellichero et al. (2018).

#### 2.4. Other Data

We determine the sea ice edge using gridded daily sea ice data (Spren et al., 2008). Since WW evolution is tied to sea ice dynamics, we often distinguish the SO into two domains: the under-ice zone, which we define as the region south of the 15% sea ice concentration line for the respective period that is typically associated with sea ice cover, and includes a transitional region from an area of mixed sea ice and open ocean conditions to the sea ice capped ocean; and the open-ocean zone refers to north of the 15% sea ice concentration line, which is not necessarily ice-free but is an area of mixed sea ice conditions that transitions from the sea-ice capped ocean to open ocean.

ACC boundaries of the PF and SAF were defined using absolute dynamic topography (ADT) at  $-0.58$  m and  $-0.1$  m, respectively (Park et al., 2019), using monthly altimetry data via AVISO. Shortwave radiative heat flux ( $Q_{SW}$ ) and wind stress,  $\tau$ , at monthly and  $1^\circ$  resolution from ERA5 reanalysis of the European Centre for Medium-Range Weather Forecasts (Hersbach et al., 2023) are used for the calculation of term (I) and term (III) of Equation 1, respectively, and are interpolated before use in computation.

### 3. Results and Discussion

#### 3.1. The Seasonal Cycle of Antarctic Winter Water

##### 3.1.1. Antarctic Winter Water Spatial Extent

WW forms during the sea ice formation periods of autumn and winter (Figures 4a and 4d) in the under-ice zone in the ML ( $WW_{ML}$ ) as a cold and homogeneous water mass (Figures 1a, 4a, and 4d).  $WW_{ML}$  also forms north of the 15% sea ice concentration line from ocean surface layer cooling. In winter,  $WW_{ML}$  forms a mean maximum extent of  $400 \pm 280$  km (approximately  $3.4 \pm 2.8$  degrees of latitude) north of the sea ice concentration line in the open-ocean zone. 81% of WW profiles in winter are classified as  $WW_{ML}$ , and the remainder of profiles are  $WW_{SS}$  (profiles containing a subsurface temperature minimum) in the open-ocean zone at the northern extent of WW. The  $WW_{SS}$  profiles are on average north of the southern boundary of the ACC, as shown by Jones et al. (2023), which delineates regions of differing oceanic properties, while WW profiles are largely constrained to south of the PF, as per the WW definition (Section 2.2; Figure 3).

During periods of sea ice melt (spring and summer), the ML restratifies and warms from solar heating, which overlays the remnant cold ML. Consequently, there exists a subsurface temperature minimum,  $WW_{SS}$  (Figures 1b, 4f–4h, and 4j–4l), which is sustained via salinity largely determining the density (beta ocean) (Stewart & Haine, 2016). The spring season has a heterogeneous mix of  $WW_{ML}$  and  $WW_{SS}$  classified profiles, with 68% of spring WW profiles being  $WW_{SS}$  (Figure 4b). The  $WW_{ML}$  extent retreats at different rates around the



circumpolar SO during spring; across and to the west of Kerguelen Plateau (KP) remains as a mix of  $WW_{ML}$  and  $WW_{SS}$  in the open-ocean zone, whereas the rest of the open-ocean zone is largely  $WW_{SS}$ .

The summer ocean is dominated by  $WW_{SS}$  (91% of WW profiles; Figure 4c).  $WW_{ML}$  is only found near the Antarctic continent, which are likely regions that do not form any  $WW_{SS}$  throughout the annual cycle. An example of such a region is Pine Island Bay in the Amundsen and Bellingshausen Seas (ABS), where coastal modified CDW maintains a warm subsurface ocean and the Thwaites glacier concurrently drives a cold surface layer (Dotto et al., 2022). Similarly,  $WW_{SS}$  persists throughout the annual cycle at the northernmost extent of WW domain (Figures 4a–4d and Figure S2 in Supporting Information S1), which can only be sustained through cold subsurface WW being transported northward to the regions where  $WW_{ML}$  do not form.

Surface ocean cooling and sea ice growth during autumn lead to an increase of  $WW_{ML}$  (Figure 4d), with the under-ice zone comprising almost totally of  $WW_{ML}$  and localized regions forming  $WW_{ML}$  north of the 15% sea ice concentration line. Northern portions of the under-ice zone in the Weddell Sea and Ross Sea have a mix of  $WW_{ML}$  and  $WW_{SS}$ , which is likely related to gyre circulation: cold WWs in the ML are maintained in the gyre core and edge, whereas mixing drives warmer and deeper (subsurface) WWs at gyre peripheries where the ocean transitions to ACC dynamics (Jones et al., 2023). Similarly, the northern under-ice region of the ABS has a mixed WW composition of  $WW_{ML}$  and  $WW_{SS}$ .

### 3.1.2. Antarctic Winter Water Core Thermohaline Properties

Core temperature and salinity of WW exhibit distinct seasonal cycles (Figure 5); nonetheless, both core properties exhibit large-scale spatial homogeneity in the under-ice zone (Figures 5a, 5f, 6b, and 6d). WW forms below sea ice from a cold ocean nearing freezing point, so is largely homogeneous in its mean temperature across the SO (Figure 6a), particularly in the under-ice zone (Figures 5a and 6b). Brine rejection from sea ice formation, and surface cooling drives buoyancy loss that results in a deepening of the ML (Wilson et al., 2019). Consequently, the coldest and saltiest WW is consistently observed during under-ice conditions throughout the annual cycle (Figures 5a, 5f, 6b, and 6d).

Spatially, WW core temperature in the under-ice zone remains largely homogeneous with a mean temperature of  $-1.4 \pm 0.5^\circ\text{C}$ , whereas core salinity exhibits an under-ice zone mean of  $34.23 \pm 0.16$  g/kg (Figures 6b and 6d). WW cores are substantially fresher ( $34.12 \pm 0.14$  g/kg) in the Amundsen-Bellingshausen Seas (ABS): the proximity of the ACC fronts and the eastward limb of the Ross Gyre transport CDW southward, maintaining the region as a warm shelf sea. Also, it is a region that experiences ice shelf melt and enhanced precipitation, which may play a role in the observed fresher WW core salinity in the under-ice zone (Figure 6c) (Nakayama et al., 2018; Narayanan et al., 2023; Tamsitt et al., 2021; Thompson et al., 2018). The coldest and most saline WW cores are observed within the polar gyres (approximately  $-1.5^\circ\text{C}$ , 34.6 g/kg; Figures 4a, 4f, 6a, and 6c), which are potentially maintained through salty CDW entrainment, their southern proximity and elevated sea ice production close to the Antarctic coastline. On the other hand, there is distinct variability displayed in all core properties (Figures 5–8) in the open-ocean zone when comparing properties up and downstream of large topographic features. Our findings agree with Sabu et al. (2020), who show distinctly warmer core temperatures downstream of KP; similar distinctions can be made when considering the differences in core properties up and downstream of the Southwest Indian Ridge (SWIR) and the Southeast Indian Ridge (SEIR). These differences in properties may be a consequence of topographic features stirring the downstream water column, which enhances mixing rates (Mashayek et al., 2017; Nikurashin et al., 2013; Rosso et al., 2015; Tamsitt et al., 2017) and alters the spatial gradients of WW core temperature and salinity. Nonetheless, meridional mean WW core temperatures (Figure 6a) do not differ substantially across the circumpolar SO since the formation of the temperature minimum is determined during WW formation in  $WW_{ML}$  from wintertime net ocean heat loss, so consistently approaches the freezing point (Figures 5b–5e and 6a).

Core temperature and salinity in the open-ocean zone have a strong tie to latitudinal extent, getting warmer and fresher as latitudes extend northward with a mean warming rate of  $0.14^\circ\text{C}$  per degree of latitude and decreasing in salinity at a rate of  $0.01$  g/kg per degree of latitude in the open-ocean zone (Figures 6b and 6d). Note that the latitudinal mean core salinity (Figure 6d) peaks in freshness with a large standard deviation at approximately  $70^\circ\text{S}$  ( $34.19 \pm 0.22$  g/kg); this is influenced by the fresh WW core salinities in the ABS, which is the only region that has a meridional mean salinity below  $34.2$  g/kg (Figure 6c). The mean open-ocean zone core temperature and salinity are  $0.5 \pm 0.7^\circ\text{C}$  and  $34.17 \pm 0.07$  g/kg, respectively, with the warmest and freshest cores found in the

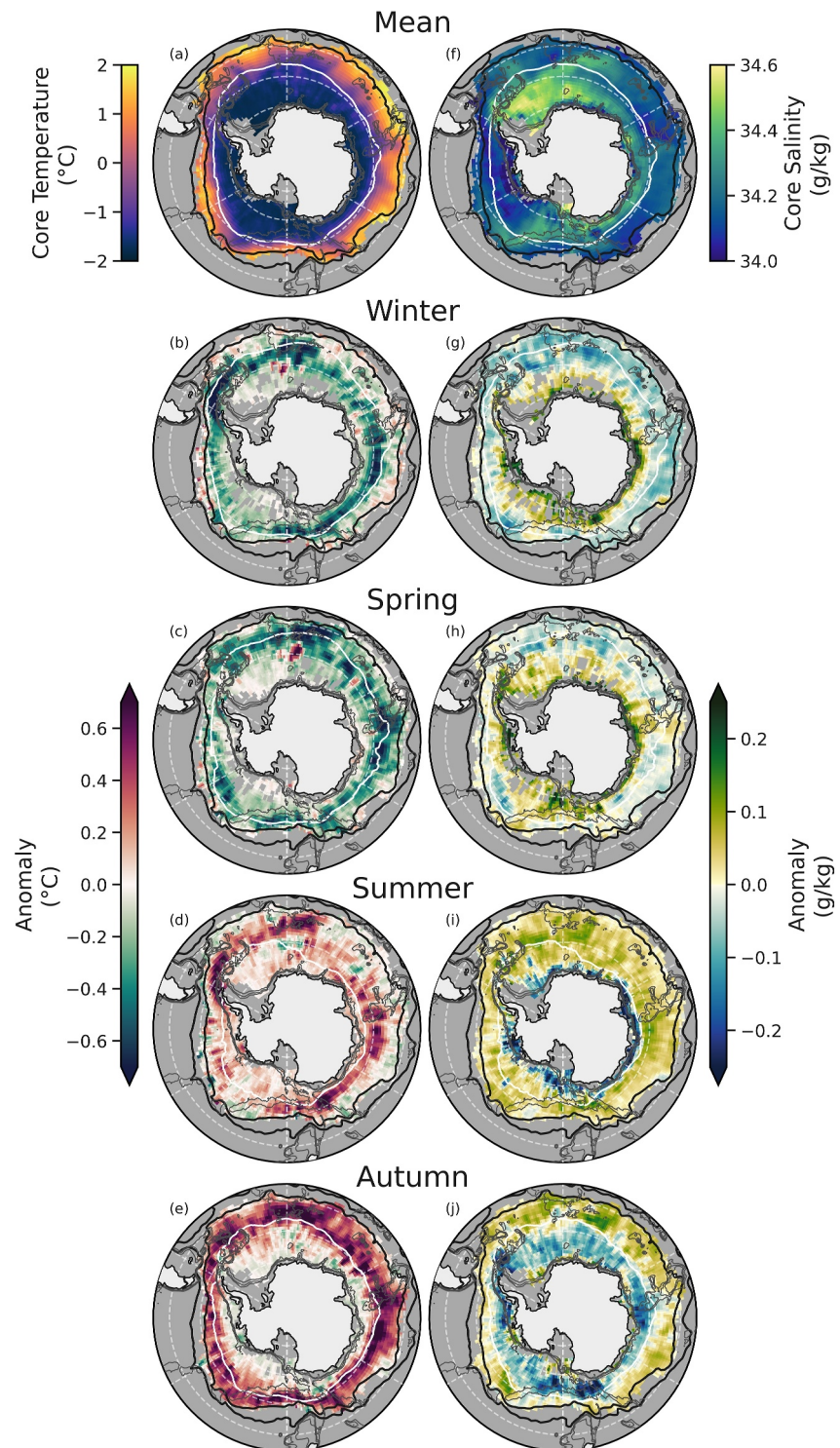


**Figure 5.** Annual mean and seasonal anomalies of Antarctic Winter Water: (a–e) core conservative temperature and (f–j) core absolute salinity. A negative (positive) anomaly implies a decrease (increase) from the annual mean. Black lines indicate the PF and SAF, white lines indicate the mean 15% sea ice concentration for the time period, and gray lines indicate 1, 2 and 3 km isobaths, and dashed white lines represent latitudes of 80, 70, 60, 50°S and longitudes of –180, –120, –60, 0, 60, 120, 180°E.

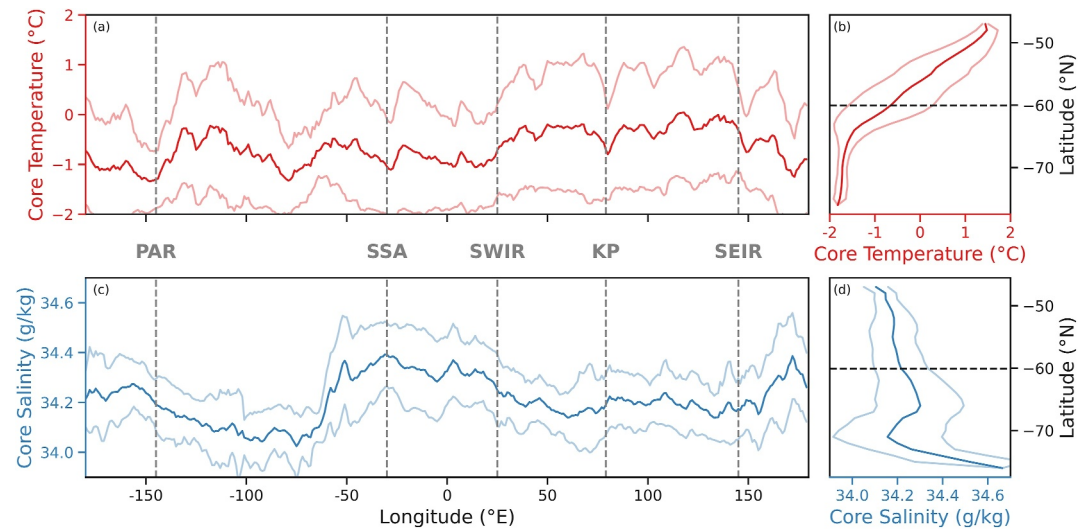


**Figure 6.** Meridional and zonal means of Antarctic Winter Water core properties. Meridional and standard deviation of panel (a) core temperature and (c) core salinity. Zonal mean and standard deviation of panel (b) core temperature and (d) core salinity. Dashed light gray vertical lines in panels (a) and (c) indicate locations of topographic features and are labeled as in Figure 2k. Dashed black horizontal lines in panels (b) and (d) indicate the location of the mean 15% sea ice concentration.

northernmost domain of WW extent ( $\sim 50^{\circ}\text{S}$ ; Figures 6b and 6d). WW core temperature and salinity properties that are typically associated with under-ice conditions (i.e., colder, more saline) extend northward into the open-ocean zone in regions that align with large topographic features, that is, Pacific-Antarctic Ridge (PAR), South Sandwich Arch (SSA), SWIR, KP, and the SEIR (Figures 5a, 5f, 6a, and 6c). Similarly, Park et al. (2009) observed a subsurface cold water tongue advected northward across the KP, which agrees with our findings.

WW core temperature exhibits large changes in temperature throughout the annual cycle, which are spatially heterogeneous (Figures 5b–5e). In winter, a net ocean-atmosphere heat loss cools the entire SO forming cold  $\text{WW}_{\text{ML}}$  below sea ice (Figure 4a). WW displays the largest seasonal temperature anomaly in winter ( $-0.5^{\circ}\text{C}$  anomaly) close to the sea ice edge, where there is the greatest change in WW core temperature throughout the annual cycle. Further, large wintertime temperature anomalies are observed in the Weddell Sea and Indian Ocean sector. The largest anomalies align with or are downstream of topographic features. These regions have elevated mixing rates (Dove et al., 2022; Mashayek et al., 2017; Mohrmann et al., 2022) so have warmer summertime WW temperatures. This thereby skews the annual mean temperature, which results in a larger magnitude anomaly signal in wintertime. Therefore, the large magnitude anomaly regions in wintertime may be representative of regions with elevated mixing rates. The ABS exhibits a smaller magnitude of temperature anomaly ( $-0.3^{\circ}\text{C}$  anomaly) in winter. Similar low magnitude temperature anomalies are observed (but positive) in the ABS during the warming season in summer (Figure 5d).

WW core temperature is at its coldest mean seasonal state in spring at  $-0.8 \pm 1.1^{\circ}\text{C}$  (Figures 5c and 5e). The sea ice begins to recede as the net heat flux becomes positive between September and October (Tamsitt et al., 2016), so the SO transitions to a  $\text{WW}_{\text{SS}}$ -dominated ocean (Figures 4b and 4c). Localized warming of WW cores initiates downstream of the Drake Passage (DP), as shown by the lower magnitude temperature anomaly (Figure 5c and Figure S3c in Supporting Information S1). This region is highly energetic, resulting in a higher rate of mixing and, thus, a faster onset of warming due to mixing with subsurface CDW and the warm surface ML (Stephenson Jr. et al., 2012). Large-scale warming of the WW core follows in summer (Figure 5d and Figure S3d in Supporting Information S1), initiated in the Atlantic and Indian Ocean sectors downstream of topographic features: DP, SSA, KP, and PAR. In the regions of deeper bathymetry and fewer topographic features (such as west of KP and in the Pacific abyssal plain), mixing rates are lower and therefore warming of WW onsets in autumn later in the seasonal cycle (Figure 5e) (Frants et al., 2013; Rosso et al., 2015; Waterhouse et al., 2014). WW across the SO in autumn is at its warmest mean core temperature at  $-0.5 \pm 1.2^{\circ}\text{C}$  due to the erosion of  $\text{WW}_{\text{SS}}$  in the open-ocean zone (Figure 5e).



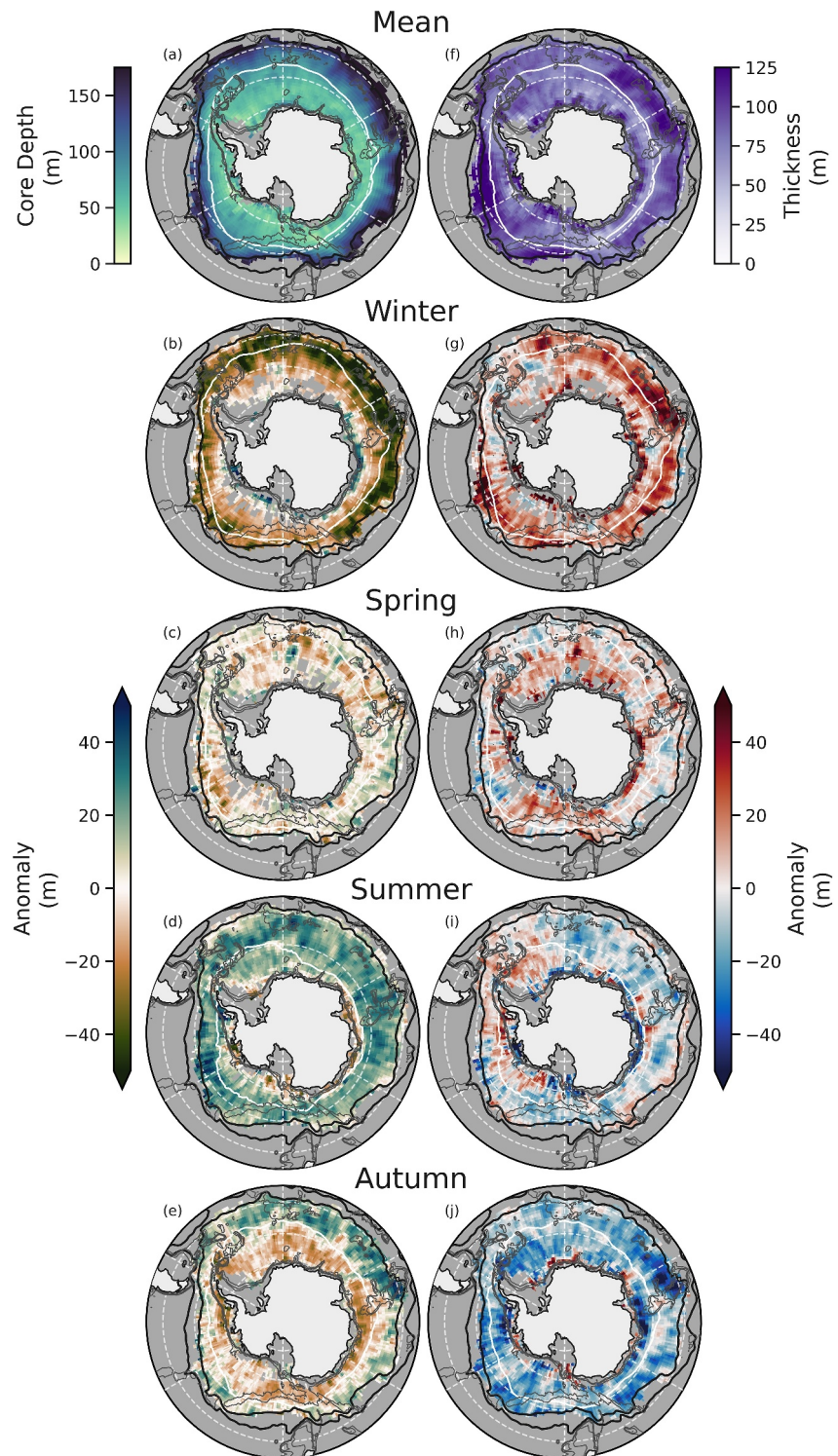


**Figure 7.** Annual mean and seasonal anomalies of Antarctic Winter Water: (a–e) core depth, and (f–j) thickness. (b–e) Core depth seasonal anomaly: positive (negative) indicates deeper (shallower) than the annual mean; (g–j) thickness anomaly: positive (negative) indicates thicker (thinner) than the annual mean. Black lines indicate the PF and SAF, white lines indicate the mean 15% sea ice concentration for the time period, and gray lines indicate 1, 2, and 3 km isobaths, and dashed white lines represent latitudes of 80, 70, 60, 50°S and longitudes of  $-180$ ,  $-120$ ,  $-60$ ,  $0$ ,  $60$ ,  $120$ ,  $180^{\circ}$ E.

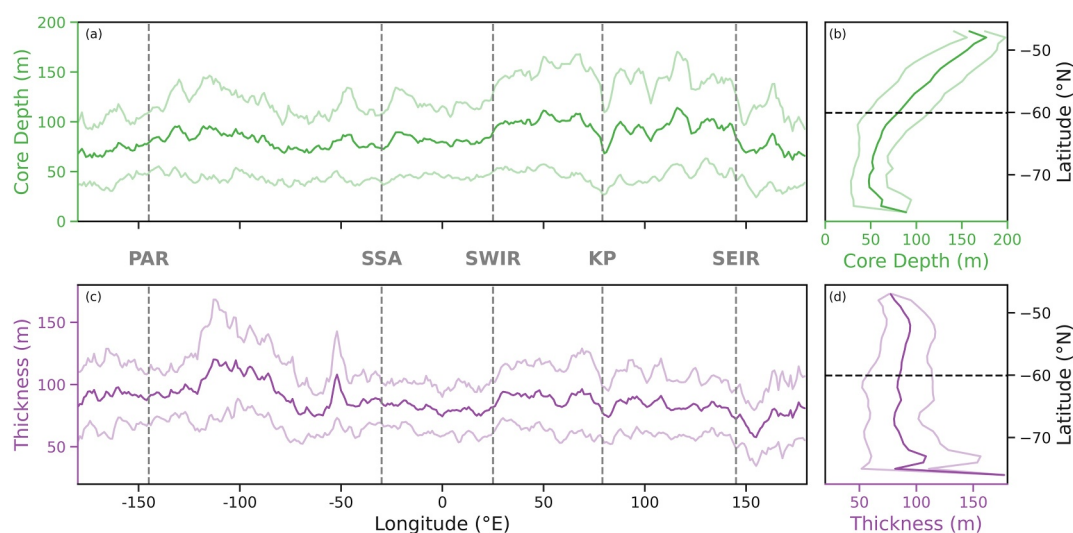


**Figure 8.** Meridional and zonal means of Antarctic Winter Water core properties. Meridional mean and standard deviation of panel (a) core depth (green) and (c) thickness (purple). Zonal mean and standard deviation of panel (b) core depth and (d) thickness. Dashed light gray vertical lines in panels (a) and (c) indicate locations of topographic features and are labeled as in Figure 2k. Dashed black horizontal lines in panels (b) and (d) indicate the location of the mean 15% sea ice concentration.

Note that there is a localized patch in the eastern Weddell Sea that has a warm mean core temperature (59°S, 7°E, Figures 5b–5e) so appears warmer throughout the winter and spring (Figures 5b and 5c). This patch aligns with a region of thin sea ice in the Weddell Gyre associated with southward CDW penetration (Holland et al., 2014; Vernet et al., 2019), which Reeve et al. (2023) show is sustained through horizontal diffusion of heat, removing heat from the southern limb of the Weddell Gyre and warming the Weddell Gyre interior.

WW core salinity (Figures 5g–5j) has a clear seasonal cycle: WW cores are fresher in winter with a seasonal mean of  $34.22 \pm 0.16$  g/kg. In winter, the WW is largely classified as residing in the ML ( $WW_{ML}$ ), which is observed as fresher than the mean core salinity since the ML is largely composed of the fresh remnant summertime ML. The southern section of the winter and spring under-ice zone has a large positive anomaly signal, which is likely due to elevated sea ice formation driving brine rejection and salinification of  $WW_{ML}$ , as shown by Haumann et al. (2016). Salinity continues to increase close to the Antarctic continent as well as in the equatorward regions in springtime (Figure 5h and Figure S3h in Supporting Information S1, which shows the seasonal difference) to the most saline period of the annual cycle with a seasonal mean WW core salinity of  $34.25 \pm 0.16$  g/kg. In summer, the circumpolar SO WW core salinity has a positive anomaly. This is driven by  $WW_{SS}$  mixing with the underlying salty CDW, which necessarily densifies WW through cabbelling via salinification (Figure 5i) (Evans et al., 2018; Groeskamp et al., 2016; Jones et al., 2023) as well as a component of salinity redistribution via advection as shown by Pellichero et al. (2018). Regions close to topographic features in summer have a greater magnitude in core salinity anomaly, for example, across the KP and along the PAR, because mixing rates are elevated and thereby increase salinification via mixing with CDW. Further, the Weddell Gyre eastward limb has an elevated summertime core salinity anomaly due to mixing with southward intruding CDW (Jones et al., 2023; Vernet et al., 2019). Around the Antarctic coastline, sea ice melt continues into summer leading to the freshening of  $WW_{ML}$  (anomaly of approximately  $-0.2$  g/kg). These localized coastal regions return to a positive anomaly in autumn (Figure 5j and Figure S3j in Supporting Information S1) potentially from an increase in salinity via sea ice formation, which likely drives the formation of  $WW_{ML}$  in the under-ice zone. The autumn under-ice zone otherwise experiences a mass freshening, which is indicative of the change from the salty and capped  $WW_{SS}$  to the fresh remnant summertime ML becoming  $WW_{ML}$ . The greatest changes in core salinity anomaly in autumn are observed in the under-ice zone, along the ABS to downstream of DP as well as along the SEIR, where there is a large change from salty  $WW_{SS}$  via mixing with CDW to fresher  $WW_{ML}$ . In the open-ocean zone, north of the sea ice edge (as defined in Section 2.4), WW remains classified as  $WW_{SS}$  and continues to increase in core salinity.

### 3.1.3. Antarctic Winter Water Core Depth and Thickness

Over the circumpolar extent, WW has a mean core depth of  $85 \pm 42$  m and a mean thickness of  $88 \pm 24$  m (Figures 7a, 7f, 8a, and 8c). The mean WW core depth is shallower under-ice, with a mean depth in the under-ice zone of  $58 \pm 21$  m (Figure 8b). Similarly, the WW layer is thinner in the under-ice zone with a mean thickness of  $84 \pm 24$  m (Figure 8d). Coastal polynya formation near the Antarctic continent results in deep WW cores and thick WW layers due to extreme heat loss and are also synonymous with more persistent WW<sub>ML</sub> conditions (Figures 4a–4d). Consequently, deep cores and thick WW layers are observed in the southern-most regions of the under-ice zone and is otherwise relatively spatially homogeneous in the meridional mean (Figures 8b and 8d). Below sea ice, submesoscale fluxes are heightened in the wintertime due to deeper mixed layers and stronger lateral gradients (Biddle & Swart, 2020). Since submesoscale fluxes are associated with enhanced vertical fluxes, which (in this region) would transport warm and salty CDW water into the WW<sub>ML</sub>, enhanced submesoscale fluxes in winter may contribute to maintaining the observed consistent WW depth and thickness in the under-ice zone. WW core depth and thickness in the open-ocean zone have a mean of  $124 \pm 34$  m and  $94 \pm 22$  m, respectively. WW core depth deepens with latitude in the open-ocean zone at an average rate of 6 m per degree of latitude northward, while thickness maintains approximately the same in the open-ocean zone. The deepest cores are found close to the PF (Figures 7a and 8b), whereas the thickest layer of WW are observed close to the Antarctic continent (Figures 7f and 8d). The average deepening of WW toward the north largely follows the deepening extent of CDW equatorward of the Antarctic shelf and can be associated with the reduced stratification and deep mixed layers associated with the PF region of the ACC (du Plessis et al., 2022). Other dominating patterns are shallower and thinner WWs near open ocean topographic features. These characteristics can be observed, for example, near the KP, SEIR as well as in the Atlantic sector near the SSA and SWIR (Figures 7a, 7f, 8a, and 8c). Deep and shallow MLs are observed up and downstream of topographic features, respectively (Figures S5a–S5e in Supporting Information S1), which directly impact WW thickness and core depth. This signal manifests itself particularly clearly in the WW thickness around KP, with a mean upstream thickness of approximately 120 m and approximately 50 m thickness directly downstream Figure 7f.

One potential explanation for the up- and downstream discrepancies of WW thickness is that regions downstream of topographic features are greater in EKE (Dove et al., 2022; Rosso et al., 2014), stirring the water column (Mashayek et al., 2017), which results in a heightened submesoscale field due to mesoscale strain via frontogenesis (McWilliams, 2021). This increases vertical mixing rates, acting to increase MLD variance in space and time and altering the depth and thickness characteristics of WW (Viglione et al., 2018) (e.g., at KP in Figure 7f). Since summertime, MLs are ubiquitously shallow across the SO (mean summertime MLD is  $41 \pm 18$  m) (Caneill et al., 2023; Dong et al., 2008; Pellichero et al., 2017), and submesoscale ML restratification takes a particular effect in winter when MLs are deep ( $114 \pm 38$  m) leading to more “patchy” spatial and temporal variability in MLD (Mahadevan & Campbell, 2002; du Plessis et al., 2017).

WW core depth (Figures 7b–7e) varies strongly seasonally (annual range of 88 m). In winter, WW is largely classified as WW<sub>ML</sub> (Figure 4a). Consequently, the shallowest core depths are observed in winter (recall that the core depth for WW<sub>ML</sub> is defined as the mid-point of the MLD; see Section 2.2 and Figure 3) with a seasonal circumpolar mean of  $70 \pm 32$  m and the largest wintertime anomaly north of the sea ice edge where the core depth has shoaled (Figure 7b and Figures S4g–S4i in Supporting Information S1). Wintertime WW cores are only observed to deepen in the under-ice zone (Figure S3l in Supporting Information S1), particularly close to the Antarctic shelf (e.g., East Antarctica). Otherwise, wintertime core depth in the under-ice zone is relatively shallow and more spatially homogeneous with a seasonal under-ice zone mean of  $55 \pm 18$  m, whereas the open-ocean zone is nearly double that with a mean winter core depth of  $105 \pm 31$  m. Spring is a transition period from a WW<sub>ML</sub>-dominated ocean to a WW<sub>SS</sub>-dominated ocean (Figure 4b and Figure S2b in Supporting Information S1). As a result, the springtime SO is a heterogeneous mix of WW<sub>ML</sub> and WW<sub>SS</sub>, particularly in the under-ice zone. Thus, the core depth deepens as WW<sub>SS</sub> becomes capped by the newly formed ML (Figure 7c and Figure S3m in Supporting Information S1) to a circumpolar mean of  $88 \pm 42$  m. WW core depth continues to deepen in summer to the deepest seasonal mean of  $98 \pm 44$  m, with a slightly greater magnitude anomaly downstream of the DP and through the Weddell Gyre. In autumn, convection drives the formation of WW<sub>ML</sub> following sea ice formation (Figure 4d), mixing the remaining WW<sub>SS</sub> into the ML and shoaling the WW core depth in the under-ice zone (Figure 7e). This shoaling leads to the largest discrepancy between mean core depth in the under-ice zone and open-ocean zone, which are  $59 \pm 21$  m and  $131 \pm 38$  m, respectively.

WW thickness displays patchiness in its seasonal cycle, thickening and thinning at different rates over the year (Figures 7g–7j and Figures S3q–S3t in Supporting Information S1). WW thickness is the thickest in winter (Figure 7g) with a circumpolar mean of  $105 \pm 30$  m, with a large positive anomaly (thicker than the mean) close to the Antarctic continent where deep MLs form as well as a patchy distribution of thick WWs north of the sea ice edge, for example, upstream of KP. WW is thicker along the continental shelf break, such as in the Pacific and Indian sectors, which agrees with the findings of deep MLs in these regions as observed by Pellichero et al. (2017). Furthermore, the low EKE region upstream of KP allows for the formation of thicker WW<sub>ML</sub>. Downstream of DP is a region of high EKE, where WW<sub>ML</sub> remains thin. In spring, the SO begins to transition to a WW<sub>SS</sub> ocean and the mean circumpolar thickness becomes  $93 \pm 22$  m.

Summer WW displays a seasonal mean of  $82 \pm 23$  m (Figure 7i). Close to the Antarctic continent, summertime WW thins with a larger magnitude due to elevated mixing along the Antarctic slope front through the WW layer, as shown by Hirano et al. (2010) in East Antarctica. Hirano et al. (2010) also computed an upward heat flux in East Antarctica that is more than double the upward heat fluxes observed in both the WS and western Peninsula shelf region (ABS). Our results of an elevated magnitude of shallowing of the WW lower boundary depth along the coastline of the Indian sector (Figure S5n in Supporting Information S1) agrees with these findings of increased heat fluxes. Further, WW is observed to reduce in thickness in the Ross Gyre in summer, which may be attributed to the seasonality in the Ross gyre circulation, with a reduced summertime gyre strength driving increased heat flux from subsurface CDW (Dotto et al., 2018). A greater magnitude anomaly of summertime WW thickening is observed in the ABS and WS (Figure S3 in Supporting Information S1). These appear to thicken due to deepening of the lower boundary (Figure S5n in Supporting Information S1), which is a signal of WW mixing with underlying CDW resulting in the max temperature gradient (i.e., the lower boundary; Figure 3) observed at a deeper depth. This postulation is supported by the core temperature increasing in summer (Figure 5d).

The seasonal mean WW thickness is observed at its thinnest in autumn with a mean of  $72 \pm 20$  m (Figure 7j). While WW close to the Antarctic continent is observed to thicken due to the formation of convective cells that contain WW<sub>ML</sub>, WW otherwise thins in the under-ice zone due to the formation of WW<sub>ML</sub>, mixing remaining WW<sub>SS</sub> with the ML (Figure 4d). In the open-ocean zone, WW remains as WW<sub>SS</sub> and erodes in thickness from continued mixing with underlying CDW as well as via deepening of the overlying surface ML (Figure 4l, and Figures S5j and S5o in Supporting Information S1).

### 3.1.4. Seasonal Heat Budget of Antarctic Winter Water

Given that temperature is the determining characteristic of the existence and classification of WW, we investigate a temperature tendency of WW<sub>SS</sub> across the annual cycle following Equation 1 (Section 2.3) to understand the mechanisms driving the distribution of WW properties and to further examine the potential link in the overturning circulation system. The temperature tendency describes the integrated heat change across the WW layer normalized by WW thickness from season to season, which we decompose into its constituent terms (Equation 1; Section 2.3). Note, in this section, we refer to the transition from autumn to winter as winter (first row in Figure 9), which represents autumn subtracted from winter, and so on.

There are several physical processes that may impact the WW<sub>SS</sub> temperature tendency (Figure 1b), including penetrative shortwave radiation, wind-driven mixing, entrainment and detrainment, WW<sub>SS</sub> subduction (via summertime restratification of the ML, capping the subsurface remnant wintertime ML) as well as WW<sub>SS</sub> obduction (via the onset of winter convection). WW<sub>SS</sub> subduction and obduction is the emergence and disappearance of WW<sub>SS</sub> from one season to the next and accounts for physical processes that may not be entirely captured by this data set due to its temporal coarseness. The former terms can be computed following Equation 1. The residual term consists of processes not accounted for by the other terms, such as diffusive convection, vertical advection, and lateral advection (Section 2.3). We take lateral advection to dominate the residual signal since diffusive convection, mean shear, and vertical advection all make small contributions to heat fluxes on these spatiotemporal scales (Bebieva & Speer, 2019; Giddy et al., 2023; van der Boog et al., 2021), whereas lateral advection is known to play a significant role in SO heat fluxes (Morrison et al., 2016).

The temperature tendency of WW<sub>SS</sub> (Figure 9) and its constituent terms (Figure S6 in Supporting Information S1) show clear seasonality. WW<sub>SS</sub> experiences an annual tendency to gain heat with an annual mean of  $0.04 \pm 1.33^\circ\text{C}$  season<sup>-1</sup> across the circumpolar SO. The mean cooling is observed in winter with a mean temperature tendency of



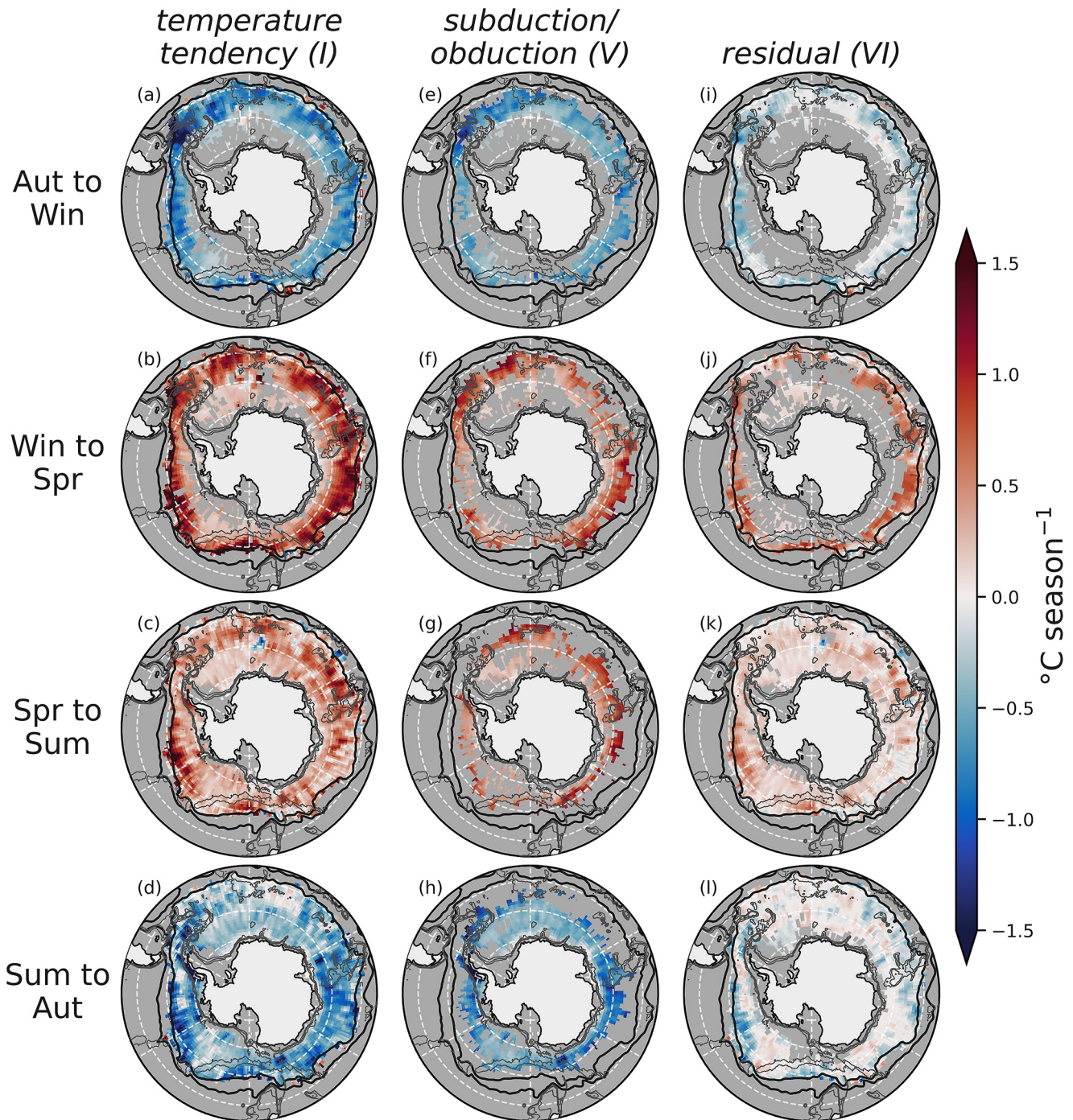


**Figure 9.** Temperature tendency of subsurface Antarctic Winter Water. (a–d) Temperature tendency where red (blue) indicates warming (cooling); (e–h)  $WW_{SS}$  subduction (red) and erosion (blue) terms; (i–l) residual where red (blue) indicates warming (cooling) via advection. The labels on the top of each row indicate the term from Equation 1. Black lines indicate the PF and SAF, gray lines indicate 1, 2, and 3 km isobaths, and dashed white lines represent latitudes of 80, 70, 60, 50°S and longitudes of -180, -120, -60, 0, 60, 120, 180°E. All terms from Equation 1 are plotted in Figure S6 in Supporting Information S1.

$-0.5 \pm 1.43^{\circ}\text{C season}^{-1}$  (Figure 9a), which is largely homogeneous. The greatest magnitude of wintertime cooling takes place downstream of the DP ( $\sim -1.8^{\circ}\text{C season}^{-1}$ ), which represents a large removal of heat from the  $WW_{SS}$  system due to the change from warm  $WW_{SS}$  to  $WW_{ML}$  (Figures 4a, 4d, and 5e). Conversely, spring has the largest mean warming of  $WW_{SS}$ , warming across the season  $0.75 \pm 1.33^{\circ}\text{C season}^{-1}$  and greater warming rates

observed in regions in close proximity to the PF which is due to the large warming driven concurrently by both subduction, inputting heat into the WW<sub>SS</sub> system, and advection, which redistributes this input heat (see more details below). Summer continues to warm WW<sub>SS</sub> at a circumpolar mean rate of  $0.38 \pm 1.06^\circ\text{C season}^{-1}$ . du Plessis et al. (2022) observe WW warming by  $\sim 1^\circ\text{C}$  over the 3 months December through February at  $60^\circ\text{S}$ ,  $0^\circ\text{E}$  with the largest changes in temperature observed across December and January (their Figure 7f), which agrees with our findings of greatest warming in spring (October to December) and continued warming in summer (January to March). In autumn, WW<sub>SS</sub> begins to cool again at a mean rate of  $-0.51 \pm 1.19^\circ\text{C season}^{-1}$ , cooling at greater magnitudes southeast of KP along the SEIR and in the DP.

The subduction and obduction of WW<sub>SS</sub> is a leading order term of temperature tendency, accounting for  $\sim 35\%$  of the annual temperature tendency budget. WW<sub>SS</sub> subduction represents the restratification of the ML following the change in sign of atmospheric heat flux to form a subsurface remnant wintertime ML. This addition of water and heat into the WW<sub>SS</sub> system thus appears as a warming of WW<sub>SS</sub> (red in Figures 9e–9h). Conversely, the obduction of WW<sub>SS</sub> results in the removal of heat from WW<sub>SS</sub> (blue in Figures 9e–9h), which can represent the erosion of WW<sub>SS</sub> or re-entrainment into the wintertime ML. During wintertime, 39% of WW profiles change from WW<sub>SS</sub> to WW<sub>ML</sub> resulting in the removal of heat from the WW<sub>SS</sub> system by a mean of  $-0.58 \pm 0.40^\circ\text{C season}^{-1}$ , accounting for 38% of the seasonal temperature tendency. In spring, the surface ocean begins to warm such that 41% of WW<sub>ML</sub> profiles become WW<sub>SS</sub> (Figure 4 and Figure S2b in Supporting Information S1), resulting in a positive temperature tendency by acting to input heat into the WW<sub>SS</sub> system with a circumpolar mean of  $0.67 \pm 0.50^\circ\text{C season}^{-1}$  and accounting for 48% of the season's temperature change. WW<sub>SS</sub> obduction in summer results in a warming of  $0.59 \pm 0.52^\circ\text{C season}^{-1}$  with smaller magnitude temperature tendency close to the Antarctic continent, such as in the Weddell Sea and Indian sector. Autumn time obduction of WW<sub>SS</sub> drives cooling of the WW<sub>SS</sub> system, especially close to the Antarctic continent in the regions where WW<sub>ML</sub> forms, for example, southeast of KP (Figure 9h). Autumn has the largest removal of heat at  $-0.68 \pm 0.49^\circ\text{C season}^{-1}$  due to the large change of WW<sub>SS</sub> to WW<sub>ML</sub> (38%), yet only accounts for % of the overall temperature tendency ( $T_{SS}$ ) for that period.

The residual, which we assume is representative of advection and refer to it as such throughout this section, is of second order importance to the temperature tendency (Figures 9i–9l). In autumn and winter, WW<sub>ML</sub> and WW<sub>SS</sub> co-exist such that deep wintertime MLs, which experience a net heat loss, reside alongside WW<sub>SS</sub>. Consequently, cold WW<sub>ML</sub> waters are advected into the WW<sub>SS</sub> and therefore cool the WW<sub>SS</sub>. Conversely, in spring and summer, the upper ocean is no longer cooling, and so WW<sub>ML</sub> is no longer forming (Figure S2 in Supporting Information S1). Therefore, advection drives warming of WW<sub>SS</sub> during spring and summer. In winter, surface cooling initiates the formation of WW<sub>ML</sub> and the subsequent equatorward advection, which results in the largest seasonal cooling of circumpolar WW<sub>SS</sub> by  $-0.20 \pm 0.47^\circ\text{C season}^{-1}$ . This advection-driven cooling is largest close to the PF at the northern extent of WW where perennial WW<sub>SS</sub> exists throughout the annual cycle (Figure S2 in Supporting Information S1). Spring WW<sub>SS</sub> has the largest magnitude mean warming via advection, warming by  $0.36 \pm 0.61^\circ\text{C season}^{-1}$ , which largely takes place close to the PF. Summer contributes to temperature tendency by warming at  $0.15 \pm 0.43^\circ\text{C season}^{-1}$  and is spatially homogeneous (Figure 9k). Advection in autumn drives cooling with a seasonal mean of  $-0.11 \pm 0.48^\circ\text{C season}^{-1}$  (Figure 9l) but is low near the Antarctic continent due to obduction of WW<sub>SS</sub> (as shown by the subduction and obduction term; Figure 9h). Spatial heterogeneity is observed in the autumn time residual term, with large magnitude signatures near KP, SEIR, and downstream of PAR.

The additional terms (II, III, and IV) of Equation 1 are presented in Figure S6 in Supporting Information S1. Overall, these terms explain the remainder of the seasonal temperature tendency. Wind-driven mixing consistently warms WW<sub>SS</sub> across the circumpolar SO throughout the seasons in agreement with the findings of Giddy et al. (2023) (Figures S6e–S6h in Supporting Information S1). The largest magnitude of WW<sub>SS</sub> warming due to wind-driven mixing occurs in autumn where there are the increased temperature gradients across the ML–WW boundary. Entrainment/detrainment varies based on the balance between warm CDW entrained into WW from below, driving warming, and heat removed from the WW layer through entrainment into the ML, thus cooling WW<sub>SS</sub>. Substantial heterogeneous cooling of WW<sub>SS</sub> due to entrainment takes place in autumn in regions void of topographic features. This is coherent with deeper ML formation by ocean surface layer heat loss during autumn, particularly in the subantarctic ocean (Pellichero et al., 2017), driving entrainment of WW into the ML and the loss of heat from WW<sub>SS</sub>.

The temperature tendency (Figure 9) provides key information to understand the seasonal change of WW<sub>SS</sub>. We show that the cooling of WW<sub>SS</sub> takes place in autumn and winter while warming and mixing with the subsurface takes place in spring and summer, indicating the seasonal nature of heat fluxes in the upper SO and is potentially significant in water mass transformation (Abernathey et al., 2016; Evans et al., 2018; Pellichero et al., 2018).

### 3.2. Mechanisms Governing the Spatial Distribution of Antarctic Winter Water

Mean WW properties (Sections 3.1.2 and 3.1.3; Figures 5–8) exhibit broadscale characteristics that are relatively consistent throughout all properties across the SO, that is, quasi-homogeneous properties in the under-ice zone with meridional gradients in the open-ocean zone that, typically, increase in the northward direction. However, there exist regions where properties associated with under-ice conditions appear to be transported northward toward the PF. These regions of conserved under-ice properties in the open-ocean zone typically align with topographic features and can be observed particularly clearly in the mean WW core density (Figure 9a) with dense WW cores in the open-ocean tightly constrained to the following topographic features: PAR, SSA, SWIR, KP, and SEIR (west to east). In order to further investigate the spatial drivers of the large-scale properties of WW, we transform WW core density from latitude-longitude coordinate space to ADT-longitude space (Figure 9c).

The distribution of WW is largely constrained to along-stream transport (referring to along-ADT streamlines). East of the PAR to the DP, in the open ocean ABS, WW is lighter in density ( $27.24 \pm 0.10 \text{ kg m}^{-3}$ ) and tightly constrained to ADT contours—a region where there is deep ocean bathymetry and few topographic features (the Pacific abyssal plane). Therefore, ocean interior mixing rates are lower than other parts of the SO (Frants et al., 2013; Ledwell et al., 2011). Thus, we posit that there are potentially reduced rates of mixing between WW and underlying CDW, which may result in the observed lighter density classes of WW in the Pacific sector. Furthermore, CDW intrusions onto the ABS continental shelf results in a warm shelf basin (Narayanan et al., 2023; Tamsitt et al., 2021). Consequently, melt rates of sea ice are elevated in the region, as shown by the regionally fresh WW cores (see Section 3.1.2; Figures 5f and 8c). In the SO, salinity is the dominating contributor toward density (Roquet et al., 2022; Stewart & Haine, 2016). Thus, fresh WW cores lead to light WW core densities in the ABS.

Conversely, the Weddell Sea region is characterized by denser WW cores ( $27.43 \pm 0.17 \text{ kg m}^{-3}$ , Figure 10) that advect northward out of the Weddell Sea and across streamlines of SSH, following the southward edge of the SSA. Locations of across-stream transport align with topographic features throughout the SO, with the strongest across-stream signal observed at the SWIR (Figure 10c). The locations of elevated WW density extending equatorward reflect the pathways of northward sea ice export (Haumann et al., 2016) and can potentially play a critical role in redistributing CDW and sea ice-driven brine properties. Further, WW core density reflects the northward advection of surface waters from the Weddell Sea where the SSA is a region known for high rates of surface advection, as is reflected by iceberg pathways (Budge & Long, 2018), and understood in observational studies via the use of the geostrophic thermal wind relation (Katsumata & Yoshinari, 2010; Oke et al., 2022).

Dense WW extending northward is observed close to the SWIR, which is likely a result of the Weddell Gyre northward circulation advecting WW northward. Similarly, dense WW is transported northward across the PAR, which is facilitated by the Ross Gyre; Zilberman et al. (2017) show similar findings of equatorward transport of ocean interior water masses such as Subantarctic Mode Water north of the ACC. Moreover, the regions of across-stream transport of WW coincide with the bathymetrically steered export pathways of Antarctic Bottom Water, as detailed by Solodoch et al. (2022) as well as others (Kusahara et al., 2017; Meredith, 2013; van Sebille et al., 2013). This also agrees with property transport preferentially facilitated by transient eddies, which are more probable to be present in regions of large bathymetric features and high EKE (Naveira Garabato et al., 2011; Thompson & Sallée, 2012; Wilson et al., 2022). Klocker et al. (2023) show that the high latitude SO pycnocline subducts into the ocean interior close to the PF to eventually form Antarctic Intermediate Waters. The density classes of the pycnocline described by Klocker et al. (2023) correspond to the observed WW core density range, highlighting the potential role that WW plays to connect the high latitude SO to the ocean interior in the over-turning circulation system.



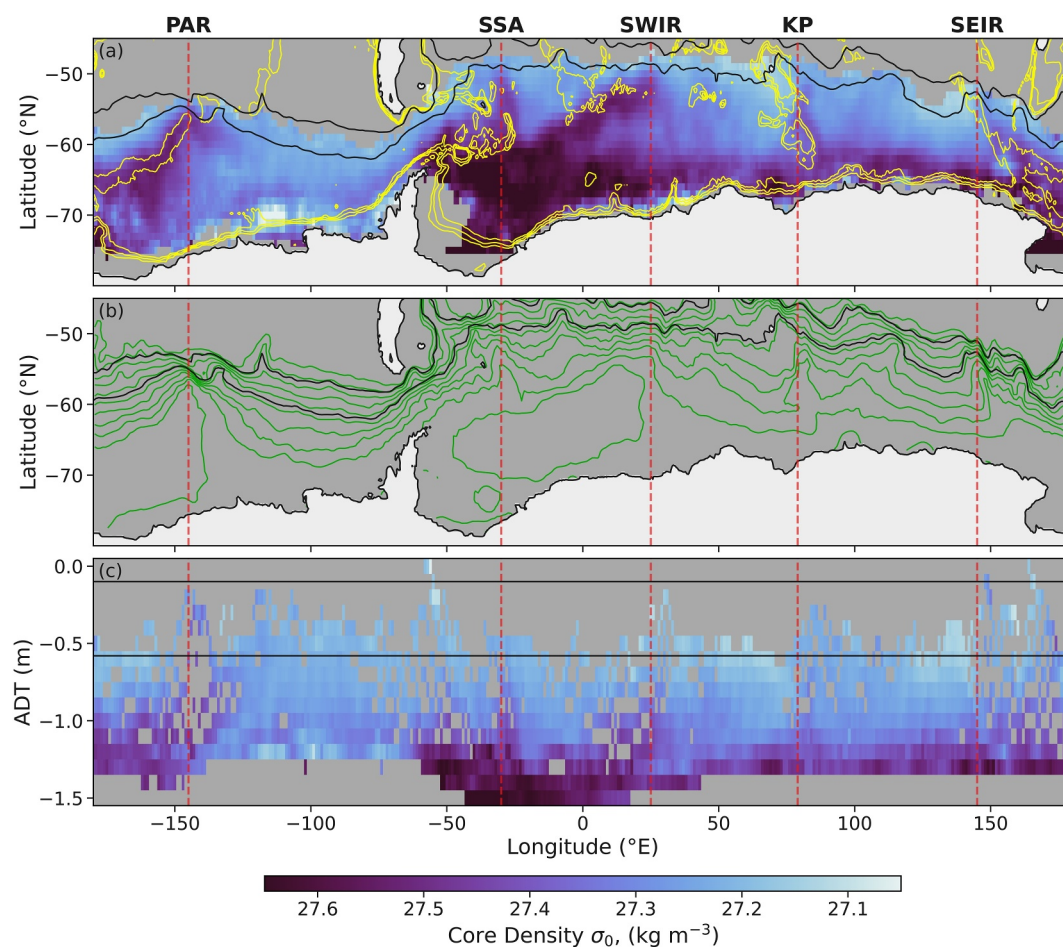


**Figure 10.** Antarctic Winter Water (WW) core density. (a) Annual mean WW core density. Yellow contours indicate 1, 2, and 3 km isobaths. (b) Absolute dynamic topography streamlines are depicted in green. (c) Annual mean WW core density mapped onto ADT-Longitude coordinate space. (a–c) Black lines indicate the PF and SAF, and vertical dashed red lines show regions of topographic features, which are labeled as in Figure 2.

## 4. Assumptions and Limitations

### 4.1. Data Limitations

Hydrographic data in the SO is prone to patchy spatiotemporal distributions (Figures 2a–2d and 2i). Certain regions have low data coverage, such as the Pacific sector and within the seasonal ice zone. Many factors impact the distribution of data, for example, ship transects determine ship-based CTD cast time and location as well as float deployments. Also, floats being largely Lagrangian are steered and entrained by the dominant ACC fronts (Figures 2e–2h), which leads to a somewhat reduced sampling of inter-frontal zones subject to reduced current strengths or shallower areas due to topographic steering (Kamenkovich et al., 2017). Nonetheless, profiling floats provide impressively broad coverage of the circumpolar SO (Figure 2j). Furthermore, MEOP is an important data set that provides near full annual coverage in the southern domains of the SO and sea ice regions (Figures 2a–2h). However, seal behavior restricts broad and unbiased geographically coverage, resulting in observation hotspots (e.g., the Western Antarctic Peninsula in ABS and KP). Further, biases are introduced due to foraging preferences, since seals favor frontal peripheries and regions that experience less intense surface warming (Azarian et al., 2024; Siegelman et al., 2019). The data included coincide with the Weddell Sea polynya years of 2016 and 2017 (Figures 2g and 2i), which results in a localized sampling bias of the warm water column over Maud Rise (~65°S, 3°E) (Gülk et al., 2023; Mohrmann et al., 2022).

The ocean is also temporally variable, as noted by the differences in WW characteristics shown in the varying seasons. Certain regions, particularly the sea ice impacted ocean, have locations of limited profiles (e.g., less than



20) in the seasonal climatology of 18 years. An implication of this is that should any interannual variability exist in the WW characteristics, there is likely to be a bias toward the characteristics of the particular period sampled. Furthermore, should there be a bias in a given month sampled, for example, more profiles existed in February during the summer climatology for a given region, then there would likely be a bias toward thinner, warmer  $WW_{SS}$ , as indicated by the seasonal evolution shown in this study. Such aspects around spatiotemporal data coverage means that the characteristics of WW are not always consistently described in space and time, particularly in the permanent sea ice regions of the Weddell and Ross Seas and on parts of continental shelves. Nonetheless, to date, data coverage is at a status, which allows robust descriptions and heat budget calculations over the vast majority of circumpolar SO and at a seasonal temporal resolution. The expected increase in observations and spatial coverage, particularly due to the onset or growth of various programs, such as SOCCOM and MEOP (Figures 2i and 2j) will further narrow these observational gaps in the coming years to better resolve aspects around interannual variability or finer scale processes modulating WW.

#### 4.2. Heat Budget Methodology

The heat budget work we have conducted provides information, for the first time, of the role  $WW_{SS}$  plays in redistributing heat in the upper SO and how this varies seasonally (Section 3.1.4). Below, we cover the assumptions made in the heat budget computation and methodology (Section 2.3). When calculating the downward turbulent heat flux (Term III), Equation 1), we use the correlation found by Nicholson et al. (2022) between theoretical dissipation and observed summertime dissipation. Thus, we make the assumption that this correlation holds for the circumpolar SO across the annual cycle. The seasonal period is important because buoyancy plays a minor role in internal mixing in the summer period due to stratifying the water column whereas buoyancy destratifies the ML and drives convection in winter, resulting in both convection and shear driving the dissipation of turbulent kinetic energy (Sohail et al., 2018). Since, we only apply our diffusivity parameterization to the open-ocean zone (north of the 15% sea ice concentration) and to  $WW_{SS}$ , the wintertime mixing terms contributes a small portion of the heat budget (<10% for winter; Figure S6 in Supporting Information S1). Nonetheless, we find our diffusivity results to be comparable across the SO, which is of the  $O(10^{-5})$  (Wu et al., 2011). Furthermore, localized results agree with observations up and downstream of DP, where mixing regimes differ due to topographically enhanced mixing (Frants et al., 2013; Merrifield et al., 2016; Whalen et al., 2012). We further cross-referenced our heat budget findings with that of Giddy et al. (2023), whose mean January heat flux of  $15 \text{ W m}^{-2}$  in ( $60^\circ\text{S}, 0^\circ\text{E}$ ) from observations agrees with our estimates. Thus, while this methodology is based on assumptions with propagating uncertainties, it is a development from existing methodologies (Pellichero et al., 2017), who use a constant diffusivity term, whereas we have used a spatiotemporally varying term that, to a first approximation, takes into account spatiotemporal variation in wind forcing and ocean stratification. Additionally, the spatiotemporal scales we resolve do not allow for the computation of all terms. Advection dominates at the scales we investigate Morrison et al. (2016), but mixing has been shown to be an important term across the summer season (Giddy et al., 2023). Thus, it is important to consider that resolving at different time steps may adjust the results, particularly impacting nonlinear terms such as entrainment. Similarly, given these spatiotemporal scales, we are unable to fully resolve the temperature tendency and are therefore unable to close the tendency, resulting in a nonzero mean temperature tendency across the annual cycle of  $-0.08 \pm 0.8^\circ\text{C season}^{-1}$ .

#### 5. Conclusion

This study investigates Antarctic Winter Water (WW) across the circumpolar Southern Ocean (SO) using over 600,000 in situ hydrographic observations across 18 years (Figure 2). We evaluate the various physical mechanisms that impact the spatiotemporal distribution of WW, as conceptually portrayed in Figure 1. We have shown that the annual cycle of WW varies seasonally, with  $WW_{ML}$  formation observed largely in regions below sea ice and during periods of sea ice growth. We show that WW subducts to become capped following summertime ML restratification in seasons of sea ice melt to form  $WW_{SS}$ , which we observe in ice-free ocean (Figure 4 and Figure S2 in Supporting Information S1). Furthermore, we found that the properties of WW (core temperature, core salinity, core depth, and thickness) vary seasonally with distinct annual cycles (Figures 5 and 7). However, annual means exhibit similar spatial distributions such that WW properties are largely homogeneous below sea ice (south of the 15% sea ice concentration extent; Figures 5–7), with meridional gradients when north of sea ice. We find that WW properties associated with under-ice characteristics are transported equatorward near large topographic features, such as the Pacific-Antarctic Ridge, South Sandwich Trench, Southwest Indian Ridge, Kerguelen Plateau and

Southeast Indian Ridge. We find that these regions show dense WW that flows across SSH streamlines (Figure 10), which is indicative of elevated velocities in the equatorward direction (through the thermal wind relation), transporting subpolar properties at different rates seasonally (Figure 9). Hence, equatorward redistribution of under-ice associated WW properties is largely driven by topographic steering, agreeing with findings of bathymetrically steered export pathways of Antarctic Bottom Water (Solodoch et al., 2022). These are potential pathways that connect WW to the ocean interior along isopycnals to form Antarctic Intermediate Water, as shown by Klocker et al. (2023), with the observed WW density classification corresponding to intermediate water classifications, linking the high latitude surface SO to the global ocean in the overturning framework.

Understanding how WW connects CDW to intermediate water in the upper limb of the overturning circulation system is crucial to understand the redistribution of oceanic properties, including heat, salinity, carbon and nutrients, which directly impact the global climate and marine ecosystems, and are similarly important for closing global budgets such as heat and nutrients. This work provides a basis for future WW studies, providing insight into the mechanisms that impact the spatiotemporal distribution of WW, some of which have been inferred based on current literature and thus beg for further and direct investigation. One such example is WW-sea ice dynamics. Similarly, this study raises many questions regarding the role WW plays in the upper ocean and overturning circulation. For example, whether subpolar properties are transported to the global ocean through the energetic ACC via eddies and whether the properties are retained or mixed away. Further studies on CDW-WW interactions will help to gain an understanding of how ocean interior properties interact with the surface ocean. Critically, this work identifies potential meridional pathways for the upper limb of the overturning circulation and provides additional evidence to support heterogeneous, seasonal, and localized overturning pathways, developing from the zonal mean overturning framework.

## Data Availability Statement

All computer code and the quality controlled vertically gridded hydrographic profiles are available in open-access repositories (Spira, 2024; Spira et al., 2023). The various hydrographic data were collated from the following programs: the International Argo Program provided the Argo floats hydrographic data (<https://portal.aodn.org.au>); the marine mammal hydrographic data were sourced from the International MEOP Consortium and the national programs that contribute to it (<http://meop.net>); the Southern Ocean biogeochemical float hydrographic data were provided by SOCCOM (<https://socc.com.princeton.edu/>); the hydrographic ship-based CTD casts and glider profiles were provided by NOAA WOD (<https://www.nodc.noaa.gov/OC5/SELECT/dbsearch/dbsearch.html>). ERA5 data are generated using Copernicus Climate Change Service Information available online at [www.ecmwf.int/en/forecasts/datasets/archive-datasets/reanalysis-datasets/era5](http://www.ecmwf.int/en/forecasts/datasets/archive-datasets/reanalysis-datasets/era5). The sea-ice data are made available via <http://data.meereisportal.de/data/iup/hdf/s/>. The ADT data used to determine the fronts are generated by the Archiving, Validation, and Interpretation of Satellite Oceanographic data service of Centre National D'Etudes Spatiales available online [www.aviso.altimetry.fr/en/data/data-access/gridded-data-extraction-tool.html](http://www.aviso.altimetry.fr/en/data/data-access/gridded-data-extraction-tool.html). Bathymetry data is available by GEBCO Compilation Group (GEBCO, 2023).

## References

- Abernathey, R., Marshall, J., & Ferreira, D. (2011). The dependence of Southern Ocean meridional overturning on wind stress. *Journal of Physical Oceanography*, 41(12), 2261–2278. <https://doi.org/10.1175/jpo-d-11-023.1>
- Abernathey, R. P., Cerovecki, I., Holland, P. R., Newsom, E., Mazloff, M., & Talley, L. D. (2016). Water-mass transformation by sea ice in the upper branch of the Southern Ocean overturning. *Nature Geoscience*, 9(8), 596–601. <https://doi.org/10.1038/ngeo2749>
- Azarian, C., Bopp, L., Sallée, J.-B., Swart, S., Guinet, C., & d'Ovidio, F. (2024). Marine heatwaves and global warming impacts on winter waters in the Southern Indian Ocean. *Journal of Marine Systems*, 243, 103962. <https://doi.org/10.1016/j.jmarsys.2023.103962>
- Bebieva, Y., & Speer, K. (2019). The regulation of sea ice thickness by double-diffusive processes in the Ross Gyre. *Journal of Geophysical Research: Oceans*, 124(10), 7068–7081. <https://doi.org/10.1029/2019JC015247>
- Belkin, I. M., & Gordon, A. L. (1996). Southern Ocean fronts from the Greenwich meridian to Tasmania. *Journal of Geophysical Research*, 101(C2), 3675–3696. <https://doi.org/10.1029/95JC02750>
- Biddle, L. C., & Swart, S. (2020). The observed seasonal cycle of submesoscale processes in the Antarctic marginal ice zone. *Journal of Geophysical Research: Oceans*, 125(6). <https://doi.org/10.1029/2019JC015587>
- Bouffard, D., & Boegman, L. (2013). A diapycnal diffusivity model for stratified environmental flows. *Dynamics of Atmospheres and Oceans*, 61–62, 14–34. <https://doi.org/10.1016/j.dynatmoce.2013.02.002>
- Boyer, T., Baranova, C., Coleman, H. E., Garcia, A., Grodsky, R. A., & Locarnini, A. V. (2018). World Ocean Database 2018 [Dataset]. <http://wod.iode.org/SELECT/dbsearch/dbsearch.html>
- Boyer, T., Zhang, H.-M., O'Brien, K., Reagan, J., Diggs, S., Freeman, E., et al. (2023). Effects of the pandemic on observing the global ocean. *Bulletin of the American Meteorological Society*, 104(2), E389–E410. <https://doi.org/10.1175/bams-d-21-0210.1>

## Acknowledgments

We would like to acknowledge the significant efforts made to collect the various public access hydrographic observations made available by programs such as Argo, MEOP, SOCCOM, WOD18, and glider and ship-based campaigns that we use in this study. Argo data were collected and made freely available by the International Argo Program and the national programs that contribute to it (<https://argo.ucsd.edu>, <https://www.ocean-ops.org>). SOCCOM data were collected and made freely available by the Southern Ocean Carbon and Climate Observations and Modeling (SOCCOM) Project by the National Science Foundation, Division of Polar Programs (NSF PLR - 1425989 and OPP-1936222 and 2332379), supplemented by NASA, and by the International Argo Program and the NOAA programs that contribute to it. The Argo Program is part of the Global Ocean Observing System. The marine mammal data were collected and made freely available by the International MEOP Consortium and the national programs that contribute to it (<https://www.meop.net>). T. S and S.S are supported by S.S. by a Wallenberg Academy Fellowship (WAF 2015.0186) and the Swedish Research Council (VR 2019–04400) Grant S.S. and M.D.d.P. have received funding from the European Union's Horizon 2020 research and innovation program under Grant 821001 (SO-CHIC). M.D.d.P. is supported by the European Union's Marie Skłodowska Curie Individual Fellowship under Project ID 101032683. I.G. is supported by the Post Doctoral Fellowship grant of the Swedish Research Council (2022-00395).

- Brett, A., Leape, J., Abbott, M., Sakaguchi, H., Cao, L., Chand, K., et al. (2020). Ocean data need a sea change to help navigate the warming world. *Nature*, 582(7811), 181–183. <https://doi.org/10.1038/d41586-020-01668-z>
- Budge, J. S., & Long, D. G. (2018). A Comprehensive Database for Antarctic iceberg tracking using scatterometer data. *Ieee Journal of Selected Topics in Applied Earth Observations and Remote Sensing*, 11(2), 434–442. <https://doi.org/10.1109/JSTARS.2017.2784186>
- Caneill, R., Roquet, F., & Nycander, J. (2023). Southern Ocean deep mixing band emerges from a competition between winter buoyancy loss and upper stratification strength. *EGUsphere*, 2023, 1–29. <https://doi.org/10.5194/egusphere-2023-2404>
- Caneill, R., Roquet, F., & Nycander, J. (2024). The Southern Ocean deep mixing band emerges from a competition between winter buoyancy loss and upper stratification strength. *Ocean Science*, 20(2), 601–619. <https://doi.org/10.5194/os-20-601-2024>
- de Boyer Montégut, C., Madec, G., Fischer, A. S., Lazar, A., & Iudicone, D. (2004). Mixed layer depth over the global ocean: An examination of profile data and a profile-based climatology. *Journal of Geophysical Research*, 109(C12), C12003. <https://doi.org/10.1029/2004JC002378>
- Dohan, K., & Davis, R. E. (2011). Mixing in the transition layer during two storm events. *Journal of Physical Oceanography*, 41(1), 42–66. <https://doi.org/10.1175/2010Jpo4253.1>
- Dong, S., Sprintall, J., Gille, S. T., & Talley, L. (2008). Southern Ocean mixed-layer depth from Argo float profiles. *Journal of Geophysical Research*, 113(C6), C06013. <https://doi.org/10.1029/2006JC004051>
- Dotto, T. S., Heywood, K. J., Hall, R. A., Scambos, T. A., Zheng, Y., Nakayama, Y., et al. (2022). Ocean variability beneath Thwaites Eastern Ice Shelf driven by the Pine Island Bay Gyre strength. *Nature Communications*, 13(1), 7840. <https://doi.org/10.1038/s41467-022-35499-5>
- Dotto, T. S., Naveira Garabato, A., Bacon, S., Tsamados, M., Holland, P. R., Hooley, J., et al. (2018). Variability of the Ross Gyre, Southern Ocean: Drivers and responses revealed by satellite altimetry. *Geophysical Research Letters*, 45(12), 6195–6204. <https://doi.org/10.1029/2018GL078607>
- Dove, L. A., Balwada, D., Thompson, A. F., & Gray, A. R. (2022). Enhanced ventilation in energetic regions of the Antarctic Circumpolar Current. *Geophysical Research Letters*, 49(13), e2021GL097574. <https://doi.org/10.1029/2021GL097574>
- Drake, H. F., Morrison, A. K., Griffies, S. M., Sarmiento, J. L., Weijer, W., & Gray, A. R. (2018). Lagrangian timescales of Southern Ocean upwelling in a hierarchy of model resolutions. *Geophysical Research Letters*, 45(2), 891–898. <https://doi.org/10.1002/2017GL076045>
- du Plessis, M., Swart, S., Ansong, I. J., & Mahadevan, A. (2017). Submesoscale processes promote seasonal restratification in the Subantarctic Ocean. *Journal of Geophysical Research: Oceans*, 122(4), 2960–2975. <https://doi.org/10.1002/2016JC012494>
- du Plessis, M., Swart, S., Biddle, L. C., Giddy, I. S., Monteiro, P. M. S., Reason, C. J. C., et al. (2022). The daily-resolved Southern Ocean mixed layer: Regional contrasts assessed using glider observations. *Journal of Geophysical Research: Oceans*, 127(4), e2021JC017760. <https://doi.org/10.1029/2021JC017760>
- Evans, D. G., Zika, J. D., Naveira Garabato, A. C., & Nurser, A. J. G. (2018). The cold transit of Southern Ocean upwelling. *Geophysical Research Letters*, 45(24), 13386–13395. <https://doi.org/10.1029/2018GL079986>
- Frants, M., Damerell, G. M., Gille, S. T., Heywood, K. J., MacKinnon, J., & Sprintall, J. (2013). An assessment of density-based finescale methods for estimating diapycnal diffusivity in the Southern Ocean. *Journal of Atmospheric and Oceanic Technology*, 30(11), 2647–2661. <https://doi.org/10.1175/JTECH-D-12-00241.1>
- Ganachaud, A., & Wunsch, C. (2000). Improved estimates of global ocean circulation, heat transport and mixing from hydrographic data. *Nature*, 408(6811), 453–457. <https://doi.org/10.1038/35044048>
- GEBCO. (2023). GEBCO 2023 grid [Dataset]. *GEBCO Compilation Group*. <https://doi.org/10.5285/f98b053b-6100cbc-6c23-e053-6c86abc0af7b>
- Giddy, I. S., Fer, I., Swart, S., & Nicholson, S.-A. (2023). Vertical convergence of turbulent and double-diffusive heat flux drives warming and erosion of Antarctic Winter Water in summer. *Journal of Physical Oceanography*, 53(8), 1941–1958. <https://doi.org/10.1175/JPO-D-22-0259.1>
- Goosse, H., Allende Contador, S., Bitz, C. M., Blanchard-Wrigglesworth, E., Eayrs, C., Fichefet, T., et al. (2023). Modulation of the seasonal cycle of the Antarctic sea ice extent by sea ice processes and feedbacks with the ocean and the atmosphere. *The Cryosphere*, 17(1), 407–425. <https://doi.org/10.5194/tc-17-407-2023>
- Gordon, A. L., & Huber, B. A. (1984). Thermohaline stratification below the Southern Ocean sea ice. *Journal of Geophysical Research*, 89(C1), 641–648. <https://doi.org/10.1029/jc089c01p00641>
- Gordon, A. L., & Huber, B. A. (1990). Southern Ocean winter mixed layer. *Journal of Geophysical Research*, 95(C7), 11655–11672. <https://doi.org/10.1029/JC095c07p11655>
- Gregg, M., D'Asaro, E., Riley, J., & Kunze, E. (2018). Mixing efficiency in the ocean. *Annual Review of Marine Science*, 10(1), 443–473. <https://doi.org/10.1146/annurev-marine-121916-063643>
- Groeskamp, S., Abernathy, R. P., & Klocker, A. (2016). Water mass transformation by cabbeling and thermobaricity. *Geophysical Research Letters*, 43(20), 10835–10845. <https://doi.org/10.1002/2016GL070860>
- Gülk, B., Roquet, F., Naveira Garabato, A. C., Narayanan, A., Rousset, C., & Madec, G. (2023). Variability and remote controls of the warm-water halo and taylor cap at Maud Rise. *Journal of Geophysical Research: Oceans*, 128(7), e2022JC019517. <https://doi.org/10.1029/2022JC019517>
- Haumann, F. A., Gruber, N., Münnich, M., Frenger, I., & Kern, S. (2016). Sea-ice transport driving Southern Ocean salinity and its recent trends. *Nature*, 537(7618), 89–92. <https://doi.org/10.1038/nature19101>
- Hersbach, H., Bell, B., Berrisford, P., Biavati, G., Horányi, A., Muñoz Sabater, J., et al. (2023). ERA5 monthly averaged data on single levels from 1940 to present. *Copernicus Climate Change Service (C3S) Climate Data Store (CDS)*. <https://doi.org/10.24381/cds.f17050d7>
- Hirano, D., Kitade, Y., Nagashima, H., & Matsuyama, M. (2010). Characteristics of observed turbulent mixing across the Antarctic Slope Front at 140°E, East Antarctica. *Journal of Oceanography*, 66(1), 95–104. <https://doi.org/10.1007/s10872-010-0008-x>
- Holland, P. R. (2014). The seasonality of Antarctic sea ice trends. *Geophysical Research Letters*, 41(12), 4230–4237. <https://doi.org/10.1002/2014GL060172>
- Holland, P. R., Bruneau, N., Enright, C., Losch, M., Kurtz, N. T., & Kwok, R. (2014). Modeled trends in Antarctic sea ice thickness. *Journal of Climate*, 27(10), 3784–3801. <https://doi.org/10.1175/JCLI-D-13-00301.1>
- Hoppema, M., Fahrback, E., Schröder, M., Wisotzki, A., & de Baar, H. J. (1995). Winter-summer differences of carbon dioxide and oxygen in the Weddell Sea surface layer. *Marine Chemistry*, 51(3), 177–192. [https://doi.org/10.1016/0304-4203\(95\)00065-8](https://doi.org/10.1016/0304-4203(95)00065-8)
- Huguenin, M. F., Holmes, R. M., & England, M. H. (2022). Drivers and distribution of global ocean heat uptake over the last half century. *Nature Communications*, 13(1), 4921. <https://doi.org/10.1038/s41467-022-32540-5>
- Jacobs, S. S. (2004). Bottom water production and its links with the thermohaline circulation. *Antarctic Science*, 16(4), 427–437. <https://doi.org/10.1017/S095410200400224X>
- Johnson, G. C. (2008). Quantifying Antarctic Bottom Water and North Atlantic Deep Water volumes. *Journal of Geophysical Research*, 113(C5), C05027. <https://doi.org/10.1029/2007JC004477>

- Jones, D. C., Sonnewald, M., Zhou, S., Hausmann, U., Meijers, A. J. S., Rosso, I., et al. (2023). Unsupervised classification identifies coherent thermohaline structures in the Weddell Gyre region. *Ocean Science*, *19*(3), 857–885. <https://doi.org/10.5194/os-19-857-2023>
- Kamenkovich, I., Haza, A., Gray, A. R., Dufour, C. O., & Garraffo, Z. (2017). Observing system simulation experiments for an array of autonomous biogeochemical profiling floats in the Southern Ocean. *Journal of Geophysical Research: Oceans*, *122*(9), 7595–7611. <https://doi.org/10.1002/2017JC012819>
- Katsumata, K., & Yoshinari, H. (2010). Uncertainties in global mapping of Argo drift data at the parking level. *Journal of Oceanography*, *66*(4), 553–569. <https://doi.org/10.1007/s10872-010-0046-4>
- Klocker, A., Naveira Garabato, A. C., Roquet, F., de Lavergne, C., & Rintoul, S. R. (2023). Generation of the internal pycnocline in the subpolar Southern Ocean by wintertime sea ice melting. *Journal of Geophysical Research: Oceans*, *128*(3), e2022JC019113. <https://doi.org/10.1029/2022JC019113>
- Kusahara, K., Williams, G. D., Tamura, T., Massom, R., & Hasumi, H. (2017). Dense Shelf Water spreading from Antarctic coastal polynyas to the deep Southern Ocean: A regional circumpolar model study. *Journal of Geophysical Research: Oceans*, *122*(8), 6238–6253. <https://doi.org/10.1002/2017JC012911>
- Ledwell, J. R., Laurent, L. C. S., Girtton, J. B., & Toole, J. M. (2011). Diapycnal mixing in the Antarctic Circumpolar Current. *Journal of Physical Oceanography*, *41*(1), 241–246. <https://doi.org/10.1175/2010JPO4557.1>
- Lin, X., Zhai, X., Wang, Z., & Munday, D. R. (2018). Mean, variability, and trend of Southern Ocean wind stress: Role of wind fluctuations. *Journal of Climate*, *31*(9), 3557–3573. <https://doi.org/10.1175/JCLI-D-17-0481.1>
- Lund, D. C., Chase, Z., Kohfeld, K. E., & Wilson, E. A. (2021). Tracking Southern Ocean sea ice extent with Winter Water: A new method based on the oxygen isotopic signature of foraminifera. *Paleoceanography and Paleoclimatology*, *36*(6), e2020PA004095. <https://doi.org/10.1029/2020PA004095>
- Mahadevan, A., & Campbell, J. W. (2002). Biogeochemical patchiness at the sea surface. *Geophysical Research Letters*, *29*(19), 32–1–32–4. <https://doi.org/10.1029/2001GL014116>
- Marshall, J., & Speer, K. (2012). Closure of the meridional overturning circulation through Southern Ocean upwelling. *Nature Geoscience*, *5*(3), 171–180. <https://doi.org/10.1038/ngeo1391>
- Martinson, D. G. (1990). Evolution of the Southern Ocean winter mixed layer and sea ice: Open ocean deepwater formation and ventilation. *Journal of Geophysical Research*, *95*(C7), 11641–11654. <https://doi.org/10.1029/JC095iC07p11641>
- Mashayek, A., Ferrari, R., Merrifield, S., Ledwell, J. R., St Laurent, L., & Garabato, A. N. (2017). Topographic enhancement of vertical turbulent mixing in the Southern Ocean. *Nature Communications*, *8*(1), 14197. <https://doi.org/10.1038/ncomms14197>
- McMahon, C. R., Hindell, M. A., Charrassin, J.-B., Corney, S., Guinet, C., Harcourt, R., et al. (2019). Finding mesopelagic prey in a changing Southern Ocean. *Scientific Reports*, *9*(1), 19013. <https://doi.org/10.1038/s41598-019-55152-4>
- McWilliams, J. C. (2021). Oceanic frontogenesis. *Annual Review of Marine Science*, *13*(1), 227–253. <https://doi.org/10.1146/annurev-marine-032320-120725>
- Meredith, M. P. (2013). Replenishing the abyss. *Nature Geoscience*, *6*(3), 166–167. <https://doi.org/10.1038/ngeo1743>
- Merrifield, S. T., Laurent, L. S., Owens, B., Thurnherr, A. M., & Toole, J. M. (2016). Enhanced diapycnal diffusivity in intrusive regions of the Drake Passage. *Journal of Physical Oceanography*, *46*(4), 1309–1321. <https://doi.org/10.1175/JPO-D-15-0068.1>
- Mohrmann, M., Heuzé, C., & Swart, S. (2021). Southern Ocean polynyas in CMIP6 models. *The Cryosphere*, *15*(9), 4281–4313. <https://doi.org/10.5194/tc-15-4281-2021>
- Mohrmann, M., Swart, S., & Heuzé, C. (2022). Observed mixing at the flanks of Maud Rise in the Weddell Sea. *Geophysical Research Letters*, *49*(8), e2022GL098036. <https://doi.org/10.1029/2022GL098036>
- Morales Maqueda, M. A., Willmott, A. J., & Biggs, N. R. T. (2004). Polynya dynamics: A review of observations and modeling. *Reviews of Geophysics*, *42*(1). <https://doi.org/10.1029/2002RG000116>
- Morrison, A. K., Griffies, S. M., Winton, M., Anderson, W. G., & Sarmiento, J. L. (2016). Mechanisms of Southern Ocean heat uptake and transport in a global eddying climate model. *Journal of Climate*, *29*(6), 2059–2075. <https://doi.org/10.1175/JCLI-D-15-0579.1>
- Morrow, R., Valladeau, G., & Sallee, J.-B. (2008). Observed subsurface signature of Southern Ocean sea level rise. *Progress in Oceanography*, *57*(4), 351–366. <https://doi.org/10.1016/j.pocean.2007.03.002>
- Mosby, H. (1934). The waters of the Atlantic Antarctic ocean. *Scientific Research Norwegian Expedition 1927-28*, *1*(1), 1–131.
- Munk, W. H. (1966). Abyssal recipes. In *Deep Sea research and oceanographic abstracts* (Vol. 13(4), pp. 707–730). [https://doi.org/10.1016/0011-7471\(66\)90602-4](https://doi.org/10.1016/0011-7471(66)90602-4)
- Nakayama, Y., Menemenlis, D., Zhang, H., Schodlok, M., & Rignot, E. (2018). Origin of Circumpolar Deep Water intruding onto the Amundsen and Bellingshausen Sea continental shelves. *Nature Communications*, *9*(1), 3403. <https://doi.org/10.1038/s41467-018-05813-1>
- Narayanan, A., Gille, S. T., Mazloff, M. R., du Plessis, M. D., Murali, K., & Roquet, F. (2023). Zonal distribution of Circumpolar Deep Water transformation rates and its relation to heat content on Antarctic shelves. *Journal of Geophysical Research: Oceans*, *128*(6), e2022JC019310. <https://doi.org/10.1029/2022JC019310>
- Naveira Garabato, A. C., Ferrari, R., & Polzin, K. L. (2011). Eddy stirring in the Southern Ocean. *Journal of Geophysical Research*, *116*(C9), C09019. <https://doi.org/10.1029/2010JC006818>
- Nicholson, S.-A., Whitt, D. B., Fer, I., Du Plessis, M. D., Lebéhot, A. D., Swart, S., et al. (2022). Storms drive outgassing of CO<sub>2</sub> in the subpolar Southern Ocean. *Nature Communications*, *13*(1), 158. <https://doi.org/10.1038/s41467-021-27780-w>
- Nikurashin, M., Vallis, G. K., & Adcroft, A. (2013). Routes to energy dissipation for geostrophic flows in the Southern Ocean. *Nature Geoscience*, *6*(1), 48–51. <https://doi.org/10.1038/ngeo1657>
- Oke, P. R., Rykova, T., Pilo, G. S., & Lovell, J. L. (2022). Estimating argo float trajectories under ice. *Earth and Space Science*, *9*(7), e2022EA002312. <https://doi.org/10.1029/2022EA002312>
- Orsi, A. H., Whitworth, T., & Nowlin, W. D. (1995). On the meridional extent and fronts of the Antarctic Circumpolar Current. *Deep Sea Research Part I: Oceanographic Research Papers*, *42*(5), 641–673. [https://doi.org/10.1016/0967-0637\(95\)00021-W](https://doi.org/10.1016/0967-0637(95)00021-W)
- Osborn, T. R. (1980). Estimates of the local rate of vertical diffusion from dissipation measurements. *Journal of Physical Oceanography*, *10*(1), 83–89. [https://doi.org/10.1175/1520-0485\(1980\)010<0083:EOTLRO>2.0.CO;2](https://doi.org/10.1175/1520-0485(1980)010<0083:EOTLRO>2.0.CO;2)
- Park, Y.-H., Charriaud, E., & Fieux, M. (1998). Thermohaline structure of the Antarctic Surface Water/Winter Water in the Indian sector of the Southern Ocean. *Journal of Marine Systems*, *17*(1–4), 5–23. [https://doi.org/10.1016/s0924-7963\(98\)00026-8](https://doi.org/10.1016/s0924-7963(98)00026-8)
- Park, Y.-H., Charriaud, E., Pino, D. R., & Jeandel, C. (1998). Seasonal and interannual variability of the mixed layer properties and steric height at station KERFIX, southwest of Kerguelen. *Journal of Marine Systems*, *17*(1–4), 571–586. [https://doi.org/10.1016/s0924-7963\(98\)00065-7](https://doi.org/10.1016/s0924-7963(98)00065-7)
- Park, Y.-H., Park, T., Kim, T.-W., Lee, S.-H., Hong, C.-S., Lee, J.-H., et al. (2019). Observations of the Antarctic Circumpolar Current over the Udintsev Fracture Zone, the narrowest choke point in the Southern Ocean. *Journal of Geophysical Research: Oceans*, *124*(7), 4511–4528. <https://doi.org/10.1029/2019JC015024>



- Park, Y.-H., Vivier, F., Roquet, F., & Kestenare, E. (2009). Direct observations of the ACC transport across the Kerguelen Plateau. *Geophysical Research Letters*, 36(18), L18603. <https://doi.org/10.1029/2009GL039617>
- Paulson, C. A., & Simpson, J. J. (1977). Irradiance measurements in the upper ocean. *Journal of Physical Oceanography*, 7(6), 952–956. [https://doi.org/10.1175/1520-0485\(1977\)007<0952:IMITUO>2.0.CO;2](https://doi.org/10.1175/1520-0485(1977)007<0952:IMITUO>2.0.CO;2)
- Pellichero, V., Sallée, J.-B., Chapman, C. C., & Downes, S. M. (2018). The Southern Ocean meridional overturning in the sea-ice sector is driven by freshwater fluxes. *Nature Communications*, 9(1), 1789. <https://doi.org/10.1038/s41467-018-04101-2>
- Pellichero, V., Sallée, J.-B., Schmidtko, S., Roquet, F., & Charrassin, J.-B. (2017). The ocean mixed layer under Southern Ocean sea-ice: Seasonal cycle and forcing: Ocean mixed layer under southern sea-ice. *Journal of Geophysical Research: Oceans*, 122(2), 1608–1633. <https://doi.org/10.1002/2016JC011970>
- Pollard, R. T., Lucas, M. I., & Read, J. F. (2002). Physical controls on biogeochemical zonation in the Southern Ocean. *Deep Sea Research Part II: Topical Studies in Oceanography*, 49(16), 3289–3305. [https://doi.org/10.1016/S0967-0645\(02\)00084-X](https://doi.org/10.1016/S0967-0645(02)00084-X)
- Reeve, K. A., Boebel, O., Kanzow, T., Strass, V., Rohardt, G., & Fahrback, E. (2015). Objective mapping of Argo data in the Weddell Gyre: A gridded dataset of upper ocean water properties. *Earth System Science Data Discussions*, 8(1).
- Reeve, K. A., Kanzow, T., Boebel, O., Vredenburg, M., Strass, V., & Gerdes, R. (2023). The Weddell Gyre heat budget associated with the Warm Deep Water circulation derived from Argo floats. *Ocean Science*, 19(4), 1083–1106. <https://doi.org/10.5194/os-19-1083-2023>
- Roquet, F., Ferrière, D., Caneill, R., Schlesinger, D., & Madec, G. (2022). Unique thermal expansion properties of water key to the formation of sea ice on Earth. *Science Advances*, 8(46), eabq0793. <https://doi.org/10.1126/sciadv.abq0793>
- Rosso, I., Hogg, A. M., Kiss, A. E., & Gayen, B. (2015). Topographic influence on submesoscale dynamics in the Southern Ocean. *Geophysical Research Letters*, 42(4), 1139–1147. <https://doi.org/10.1002/2014GL062720>
- Rosso, I., Hogg, A. M., Strutton, P. G., Kiss, A. E., Matear, R., Klocker, A., & Van Sebille, E. (2014). Vertical transport in the ocean due to submesoscale structures: Impacts in the Kerguelen region. *Ocean Modelling*, 80, 10–23. <https://doi.org/10.1016/j.ocemod.2014.05.001>
- Sabu, P., Libera, S. A., Chacko, R., Anilkumar, N., Subeesh, M., & Thomas, A. P. (2020). Winter water variability in the Indian Ocean sector of Southern Ocean during austral summer. *Deep Sea Research Part II: Topical Studies in Oceanography*, 178, 104852. <https://doi.org/10.1016/j.dsr2.2020.104852>
- Sarmiento, J. L., Johnson, K. S., Arteaga, L. A., Bushinsky, S. M., Cullen, H. M., Gray, A. R., et al. (2023). The Southern Ocean Carbon and climate observations and modeling (SOCCOM) project: A review. *Progress in Oceanography*, 219, 103130. <https://doi.org/10.1016/j.pocean.2023.103130>
- Sharma, G. S., & Mathew, B. (1985). Hydrography and circulation off the Antarctica in the Indian Ocean region. *Journal of Earth System Science*, 94(1), 13–27. <https://doi.org/10.1007/BF02863405>
- Shaw, W. J., & Stanton, T. P. (2014). Dynamic and double-diffusive instabilities in a weak pycnocline. Part I: Observations of heat flux and diffusivity in the vicinity of Maud Rise, Weddell Sea. *Journal of Physical Oceanography*, 44(8), 1973–1991. <https://doi.org/10.1175/JPO-D-13-042.1>
- Siegelman, L., O'Toole, M., Flexas, M., Rivière, P., & Klein, P. (2019). Submesoscale ocean fronts act as biological hotspot for southern elephant seal. *Scientific Reports*, 9(1), 5588. <https://doi.org/10.1038/s41598-019-42117-w>
- SOCCOM. (2019). Southern ocean carbon and climate observations and modelling [Dataset]. (SOCCOM). Retrieved from <https://soccom.princeton.edu/>
- Sohail, T., Gayen, B., & Hogg, A. M. (2018). Convection enhances mixing in the Southern Ocean. *Geophysical Research Letters*, 45(9), 4198–4207. <https://doi.org/10.1029/2018GL077711>
- Solodoch, A., Stewart, A. L., Hogg, A. M., Morrison, A. K., Kiss, A. E., Thompson, A. F., et al. (2022). How does Antarctic Bottom Water cross the Southern Ocean? *Geophysical Research Letters*, 49(7), e2021GL097211. <https://doi.org/10.1029/2021GL097211>
- Speer, K., Rintoul, S. R., & Sloyan, B. (2000). The diabatic Deacon cell. *Journal of Physical Oceanography*, 30(12), 3212–3222. [https://doi.org/10.1175/1520-0485\(2000\)030<3212:TDDC>2.0.CO;2](https://doi.org/10.1175/1520-0485(2000)030<3212:TDDC>2.0.CO;2)
- Spira, T. (2024). Antarctic Winter Water climatology and overturning [Software]. *Github*. [https://github.com/theospira/WW\\_climatology](https://github.com/theospira/WW_climatology)
- Spira, T., du Plessis, M., & Swart, S. (2023). Processed hydrographic SO data, 2004–2021. *Zenodo*. [Dataset]. <https://doi.org/10.5281/zenodo.10258138>
- Spreen, G., Kaleschke, L., & Heygster, G. (2008). Sea ice remote sensing using AMSR-E 89-GHz channels. *Journal of Geophysical Research*, 113(C2), C02S03. <https://doi.org/10.1029/2005JC003384>
- Stephenson, G. R., Jr., Gille, S. T., & Sprintall, J. (2012). Seasonal variability of upper ocean heat content in Drake Passage. *Journal of Geophysical Research*, 117(C4), C04019. <https://doi.org/10.1029/2011JC007772>
- Stewart, K. D., & Haine, T. W. N. (2016). Thermobaricity in the transition zones between alpha and beta oceans. *Journal of Physical Oceanography*, 46(6), 1805–1821. <https://doi.org/10.1175/JPO-D-16-0017.1>
- Talley, L. (2013). Closure of the global overturning circulation through the Indian, Pacific, and Southern Oceans: Schematics and transports. *Oceanography*, 26(1), 80–97. <https://doi.org/10.5670/oceanog.2013.07>
- Tamsitt, V., Abernathy, R. P., Mazloff, M. R., Wang, J., & Talley, L. D. (2018). Transformation of deep water masses along Lagrangian upwelling pathways in the Southern Ocean. *Journal of Geophysical Research: Oceans*, 123(3), 1994–2017. <https://doi.org/10.1002/2017JC013409>
- Tamsitt, V., Drake, H. F., Morrison, A. K., Talley, L. D., Dufour, C. O., Gray, A. R., et al. (2017). Spiraling pathways of global deep waters to the surface of the Southern Ocean. *Nature Communications*, 8(1), 172. <https://doi.org/10.1038/s41467-017-00197-0>
- Tamsitt, V., England, M. H., Rintoul, S. R., & Morrison, A. K. (2021). Residence time and transformation of warm Circumpolar Deep Water on the Antarctic continental shelf. *Geophysical Research Letters*, 48(20), e2021GL096092. <https://doi.org/10.1029/2021GL096092>
- Tamsitt, V., Talley, L. D., Mazloff, M. R., & Cerovečki, I. (2016). Zonal variations in the Southern Ocean heat budget. *Journal of Climate*, 29(18), 6563–6579. <https://doi.org/10.1175/JCLI-D-15-0630.1>
- Tamura, T., Ohshima, K. I., & Nihashi, S. (2008). Mapping of sea ice production for Antarctic coastal polynyas. *Geophysical Research Letters*, 35(7). <https://doi.org/10.1029/2007GL032903>
- Thompson, A. F., & Sallée, J.-B. (2012). Jets and topography: Jet transitions and the impact on transport in the Antarctic Circumpolar Current. *Journal of Physical Oceanography*, 42(6), 956–972. <https://doi.org/10.1175/JPO-D-11-0135.1>
- Thompson, A. F., Stewart, A. L., Spence, P., & Heywood, K. J. (2018). The Antarctic Slope Current in a changing climate. *Reviews of Geophysics*, 56(4), 741–770. <https://doi.org/10.1029/2018RG000624>
- Toole, J. M. (1981). Sea ice, winter convection, and the temperature minimum layer in the Southern Ocean. *Journal of Geophysical Research*, 86(C9), 8037–8047. <https://doi.org/10.1029/JC086iC09p08037>
- Treasure, A. M., Roquet, F., Ansong, I. J., Bester, M. N., Boehme, L., Bornemann, H., et al. (2017). Marine mammals exploring the Oceans Pole to Pole: A review of the MEOP Consortium. *Oceanography*, 30(2), 132–138. <https://doi.org/10.5670/oceanog.2017.234>

- van der Boog, C. G., Dijkstra, H. A., Pietrzak, J. D., & Katsman, C. A. (2021). Double-diffusive mixing makes a small contribution to the global ocean circulation. *Communications Earth & Environment*, 2(1), 1–9. <https://doi.org/10.1038/s43247-021-00113-x>
- van Sebille, E., Spence, P., Mazloff, M. R., England, M. H., Rintoul, S. R., & Saenko, O. A. (2013). Abyssal connections of Antarctic Bottom Water in a Southern Ocean state estimate. *Geophysical Research Letters*, 40(10), 2177–2182. <https://doi.org/10.1002/grl.50483>
- Vernet, M., Geibert, W., Hoppema, M., Brown, P. J., Haas, C., Hellmer, H. H., et al. (2019). The Weddell Gyre, Southern Ocean: Present knowledge and future challenges. *Reviews of Geophysics*, 57(3), 623–708. <https://doi.org/10.1029/2018RG000604>
- Viglione, G. A., Thompson, A. F., Flexas, M. M., Sprintall, J., & Swart, S. (2018). Abrupt transitions in submesoscale structure in southern Drake Passage: Glider observations and model results. *Journal of Physical Oceanography*, 48(9), 2011–2027. <https://doi.org/10.1175/JPO-D-13-0192.1>
- von Kármán, T. (1931). Mechanische Ähnlichkeit und turbulenz. *Proceedings of the Third International Congress on Applied Mechanics*, 1, 85–93.
- Waterhouse, A. F., MacKinnon, J. A., Nash, J. D., Alford, M. H., Kunze, E., Simmons, H. L., et al. (2014). Global patterns of diapycnal mixing from measurements of the turbulent dissipation rate. *Journal of Physical Oceanography*, 44(7), 1854–1872. <https://doi.org/10.1175/JPO-D-13-0104.1>
- Whalen, C. B., Talley, L. D., & MacKinnon, J. A. (2012). Spatial and temporal variability of global ocean mixing inferred from Argo profiles. *Geophysical Research Letters*, 39(18). <https://doi.org/10.1029/2012GL053196>
- Whitworth, T., Nowlin, W. D., Orsi, A. H., Locarnini, R. A., & Smith, S. G. (1994). Weddell Sea shelf water in the Bransfield Strait and Weddell-Scotia Confluence. *Deep Sea Research Part I: Oceanographic Research Papers*, 41(4), 629–641. [https://doi.org/10.1016/0967-0637\(94\)90046-9](https://doi.org/10.1016/0967-0637(94)90046-9)
- Wilson, E. A., Riser, S. C., Campbell, E. C., & Wong, A. P. S. (2019). Winter upper-ocean stability and ice–ocean feedbacks in the sea ice–covered Southern Ocean. *Journal of Physical Oceanography*, 49(4), 1099–1117. <https://doi.org/10.1175/JPO-D-18-0184.1>
- Wilson, E. A., Thompson, A. F., Stewart, A. L., & Sun, S. (2022). Bathymetric control of subpolar gyres and the overturning circulation in the Southern Ocean. *Journal of Physical Oceanography*, 52(2), 205–223. <https://doi.org/10.1175/JPO-D-21-0136.1>
- Wong, A. P. S., Wijffels, S. E., Riser, S. C., Pouliquen, S., Hosoda, S., Roemmich, D., et al. (2020). Argo data 1999–2019: Two million temperature–salinity profiles and subsurface velocity observations from a global array of profiling floats. *Frontiers in Marine Science*, 7. <https://doi.org/10.3389/fmars.2020.00700>
- Wu, L., Jing, Z., Riser, S., & Visbeck, M. (2011). Seasonal and spatial variations of Southern Ocean diapycnal mixing from Argo profiling floats. *Nature Geoscience*, 4(6), 363–366. <https://doi.org/10.1038/ngeo1156>
- Zeilberman, N. V., Roemmich, D. H., & Gille, S. T. (2017). The East Pacific Rise current: Topographic enhancement of the interior flow in the South Pacific Ocean. *Geophysical Research Letters*, 44(1), 277–285. <https://doi.org/10.1002/2016GL069039>